


## Rotational motion of triaxially deformed nuclei studied by the microscopic angular-momentum-projection method. I. Nuclear wobbling motion

Mitsuhiro Shimada, Yudai Fujioka, Shingo Tagami, and Yoshifumi R. Shimizu

*Department of Physics, Graduate School of Science, Kyushu University, Fukuoka 819-0395, Japan*

 (Received 27 September 2017; revised manuscript received 29 November 2017; published 16 February 2018)

Rotation of triaxially deformed nucleus has been an interesting subject in the study of nuclear structure. In the present series of work, we investigate wobbling motion and chiral rotation by employing the microscopic framework of angular-momentum projection from cranked triaxially deformed mean-field states. In this first part, the wobbling motion is studied in detail. The consequences of the three-dimensional cranking are investigated. It is demonstrated that the multiple wobbling rotational bands naturally appear as a result of fully microscopic calculation. They have the characteristic properties that are expected from the macroscopic triaxial-rotor model or the phenomenological particle-triaxial-rotor model, although quantitative agreement with the existing data is not achieved. It is also found that the excitation spectrum reflects dynamics of the angular-momentum vector in the intrinsic frame of the mean field (transverse vs longitudinal wobbling). The results obtained by using the Woods-Saxon potential and the schematic separable interaction are mainly discussed, while some results with the Gogny DIS interaction are also presented.

DOI: [10.1103/PhysRevC.97.024318](https://doi.org/10.1103/PhysRevC.97.024318)

### I. INTRODUCTION

Nuclear triaxial deformation has been a long-standing issue in the field of nuclear structure [1]. It is predicted that rather a small number of nuclei are triaxially deformed in their ground states (see, e.g., Ref. [2]). Near the ground state, however, it is very difficult to confirm that a deformed nucleus has a triaxial shape. Sometimes the existence of the  $\gamma$  band is taken as evidence of triaxiality. However, its excitation energy, typically about 800 keV–1 MeV in the rare-earth-metal region, is about an order of magnitude larger than the typical rotational (first  $2^+$ ) energy and its standard interpretation is a low-lying shape vibration around the (nearly) axially symmetric shape [1].

The situation changes at high spin (see, e.g., Refs. [3–5] and references therein). In the region of the sizable amount of the angular momentum, the orientation of the angular-momentum vector relative to the intrinsic nuclear shape comes into play. Collective rotation about all three principal axes is allowed in the triaxially deformed case so that the angular-momentum vector can tilt from the principal axes, which leads to multiple-band structure called wobbling [1]. Note that the spectrum is quite different from much simpler ones in nuclei with axially symmetric deformed mean fields. In fact, the characteristic band structure of the wobbling motion has been measured first in the  $^{163}\text{Lu}$  nucleus [6] (see, e.g., Refs. [7,8] for recent theoretical review articles). Another specific rotational structure expected in triaxially deformed nuclei is the appearance of chiral doublet bands, first predicted in Ref. [9]. Their analysis is reported in the second part of this study.

It must be emphasized that these interesting types of rotational motion associated with the triaxial deformation have been predicted by phenomenological models such as the triaxial-rotor model [1] and the particle-triaxial-rotor model

[9]. It is certainly desirable to confirm that such rotational motion appears by employing a fully microscopic framework, which is the main purpose of the present work. If necessary for the description of high-spin states, we rely on the cranking procedure applied to the triaxially deformed mean field (see, e.g., Ref. [4]). In order to recover the rotational symmetry of the states, we apply the angular-momentum-projection method (see, e.g., Ref. [10]). Since almost all the symmetries except for the space inversion (parity) are broken by the triaxial mean-field state in the present investigation, an efficient method of performing the projection calculation is necessary. We employ the method developed in Ref. [11], which has been successfully applied to the study of the nuclear tetrahedral deformation [12,13], the  $\gamma$  vibration [14], and the ground-state rotational bands [15,16] in rare-earth-metal nuclei.

It is worth mentioning that the angular-momentum-projection technique has been utilized with great success by the so-called projected shell model (PSM) [17] (see also recent review articles [18,19]). Although both our approach and the PSM rely on the angular-momentum-projection technique, the basic philosophy is different: In order to improve the results for high-spin states, the multiquasiparticle configurations are successively included in the PSM basis with the goal that the shell-model configuration mixing will converge. We optimize the mean-field states as much as possible by the cranking procedure, which has been known to be a powerful method for the description of high-spin states [4]. We believe that our approach provides a good alternative to the PSM, since the cranked mean-field efficiently incorporates the important multiquasiparticle configurations.

The paper is organized as follows. We briefly present our approach in Sec. II, where it is explained how to construct the mean field and choose the Hamiltonian. In Sec. III, the wobbling band in the  $^{163}\text{Lu}$  nucleus is investigated. The differences

between recently proposed ‘‘transverse’’ and ‘‘longitudinal’’ wobbling [20] are studied in detail by our fully microscopic approach. We should admit that we are not able to obtain good agreement with existing experimental data in the present work. However, we believe that it is totally nontrivial to show that the wobbling motion naturally appears as a result of the fully microscopic calculation. Section IV is devoted to summary of the present study. Few preliminary results were already published in Ref. [21].

## II. BASIC FORMULATION

The purpose of the present work is to study, with the microscopic angular-momentum-projection method, how the characteristic rotational features of the triaxially deformed nuclei appear and what kind of properties they have. For such a purpose, it is preferable to be able to change the mean-field parameters, like the deformation parameters and the pairing gaps, arbitrarily. Therefore, we employ a model composed of the phenomenological Woods-Saxon potential and a schematic separable interaction, which has been utilized in Refs. [11, 12]. The eigenstates of rotational band are obtained by angular-momentum projection from the mean-field state  $|\Phi\rangle$ ,

$$|\Psi_{M\alpha}^I\rangle = \sum_K g_{K,\alpha}^I \hat{P}_{MK}^I |\Phi\rangle, \quad (1)$$

where the operator  $\hat{P}_{MK}^I$  is the angular-momentum projector. The amplitudes  $g_{K,\alpha}^I$  are determined by the Hill-Wheeler equation (see, e.g., Ref. [10]),

$$\sum_{K'} \mathcal{H}_{K,K'}^I g_{K',\alpha}^I = E_\alpha^I \sum_{K'} \mathcal{N}_{K,K'}^I g_{K',\alpha}^I, \quad (2)$$

with the definition of the Hamiltonian and norm kernels,

$$\left\{ \begin{array}{l} \mathcal{H}_{K,K'}^I \\ \mathcal{N}_{K,K'}^I \end{array} \right\} = \langle \Phi | \left\{ \begin{array}{l} \hat{H} \\ 1 \end{array} \right\} \hat{P}_{KK'}^I | \Phi \rangle. \quad (3)$$

For some purpose, the properly normalized amplitudes  $f_{K,\alpha}^I$  are needed instead of the amplitudes  $g_{K,\alpha}^I$ , which are defined [10] by

$$f_{K,\alpha}^I = \sum_{K'} (\sqrt{\mathcal{N}^I})_{K,K'} g_{K',\alpha}^I, \quad (4)$$

where the quantity  $\sqrt{\mathcal{N}^I}$  denotes the square-root matrix of the norm kernel, from which the zero-norm states are properly eliminated.

The Hamiltonian  $\hat{H}$  in the present work is given by

$$\hat{H} = \hat{h}_{\text{sph}} - \frac{1}{2} \chi \sum_{\lambda=2,3,4} : \hat{F}_\lambda^\dagger \cdot \hat{F}_\lambda : - \sum_{\tau=n,p} \sum_{\lambda=0,2} g_\lambda^\tau \hat{G}_\lambda^{\tau\dagger} \cdot \hat{G}_\lambda^\tau, \quad (5)$$

where the index  $\tau$  distinguishes the neutron and proton contributions. The spherical mean field is composed of the kinetic energy and Woods-Saxon potential terms,  $\hat{h}_{\text{sph}} = \sum_{\tau=n,p} (t_\tau + V_\tau)$ , and the particle-hole interaction is isoscalar,  $\hat{F}_{\lambda\mu} = \sum_{\tau=n,p} \hat{F}_{\lambda\mu}^\tau$ , with  $\hat{F}_{\lambda\mu}^\tau = \sum_{ij} \langle i | F_{\lambda\mu}^\tau | j \rangle c_i^\dagger c_j$ , while the particle-particle (or pairing channel) interaction is given

for neutrons and protons ( $\tau = n, p$ ) separately with  $\hat{G}_{\lambda\mu}^{\tau\dagger} \equiv \frac{1}{2} \sum_{ij} \langle i | G_{\lambda\mu}^\tau | j \rangle c_i^\dagger c_j^\dagger$  ( $\tilde{j}$  is the time-reversed conjugate state of  $j$ ). In previous works [11, 12], we have used different form factors for the particle-hole and the pairing channel interactions, while in the present work, we make use of a common form factor for both of them, i.e.,

$$F_{\lambda\mu}^\tau(\mathbf{r}) = G_{\lambda\mu}^\tau(\mathbf{r}) = R_{0\tau} \frac{dV_\tau^C}{dr} Y_{\lambda\mu}(\theta, \phi), \quad (6)$$

where  $V_\tau^C(r)$  is the central part of the spherical Woods-Saxon potential and  $R_{0\tau}$  is its radius parameter. We believe that this choice is more consistent, although the final results of the angular-momentum-projection calculation do not differ very much from the previous work, if the force strengths are suitably chosen. Note that the smooth cutoff of the pairing model space for the operator  $\hat{G}$  should be done in exactly the same way as in the previous work (see Refs. [11, 12] for details).

The product-type mean-field state with the pairing correlations,  $|\Phi\rangle$  in Eq. (1), is generated by the following mean-field Hamiltonian:

$$\hat{h}_{\text{mf}} = \hat{h}_{\text{def}} - \sum_{\tau=n,p} p_0^\tau (\hat{G}_{00}^{\tau\dagger} + \hat{G}_{00}^\tau) - \sum_{\tau=n,p} \lambda_\tau \hat{N}_\tau - \boldsymbol{\omega}_{\text{rot}} \cdot \hat{\mathbf{J}}. \quad (7)$$

The first term  $\hat{h}_{\text{def}} = \sum_\tau (t_\tau + V_\tau^{\text{(def)}})$  is the deformed Woods-Saxon single-particle Hamiltonian with the usual radius parametrization,

$$R(\theta, \varphi) = R_0 c_v(\{\alpha\}) \left[ 1 + \sum_{\lambda\mu} \alpha_{\lambda\mu}^* Y_{\lambda\mu}(\theta, \varphi) \right], \quad (8)$$

which describes the deformed nuclear surface at the half depth of the potential and the quantity  $c_v(\{\alpha\})$  guarantees volume conservation. It is noted that the mean-field Hamiltonian is not fully self-consistent with the two-body Hamiltonian in Eq. (5). In this work, we employ  $\lambda = 2$  and 4 deformations with the parameters  $(\beta_2, \beta_4, \gamma)$ , where the so-called Lund convention [22] is used for the sign of triaxiality parameter  $\gamma$ , which means, for example,  $\langle x^2 \rangle < \langle y^2 \rangle < \langle z^2 \rangle$  for  $0^\circ < \gamma < 60^\circ$ . Here  $\langle x^2 \rangle$  etc. are abbreviated notations of  $\langle \sum_{a=1}^A (x^2)_a \rangle$  etc., which will be also used in the following discussions. The parameter  $p_0^\tau$  in the second term in Eq. (7) fixes the strength of the monopole ( $L = 0$ ) pairing potential. The third term takes care the number conservation on average; i.e., the chemical potential  $\lambda_\tau$  is determined such that the particle number condition,  $\langle \hat{N}_\tau \rangle = N_\tau$  is satisfied. Since the form factor of the operator  $\hat{G}_{00}^\dagger$  is not the simple (usual) monopole-pairing operator,  $\hat{G}_{00}^\dagger \neq \hat{P}^\dagger \equiv \frac{1}{2} \sum_i c_i^\dagger c_i^\dagger = \sum_{i>0} c_i^\dagger c_i^\dagger$ , the parameter  $p_0^\tau$  is not the usual pairing gap,  $\Delta_\tau$ , which corresponds to the even-odd mass difference. Instead we utilize the average pairing gap,

$$\Delta_\tau \equiv p_0^\tau \langle \hat{G}_{00}^\tau \rangle / \langle \hat{P}^\tau \rangle, \quad (9)$$

which is always uniquely related to the parameter  $p_0^\tau$ . The last term in Eq. (7) is the tilted-axis cranking term [23] with three rotational frequencies,  $\boldsymbol{\omega}_{\text{rot}} = (\omega_x, \omega_y, \omega_z)$ . Since the cranking procedure is performed for any (generally tilted) rotation axis,

we can restrict the triaxial deformation parameter to the range,  $0^\circ \leq \gamma \leq 60^\circ$ .

Once the projected wave function (1) is obtained, it is straightforward to calculate the electromagnetic transition probabilities [10]. We use no effective charge for the calculation of the  $B(E2)$  values because a large model space ( $N_{\text{osc}}^{\text{max}} = 12$ ) is employed without any kind of ‘‘core.’’ The effective spin  $g$  factor of  $0.7g_{s,\text{free}}$  is adopted for both neutrons and protons for the calculation of the  $B(M1)$  values. In this way, there is no ambiguity for the calculation of these reduced transition probabilities.

We employ the parameter set of the Woods-Saxon potential proposed by Wyss [24], the values of which are listed in Ref. [25]. In Ref. [25], the wobbling motion was studied based on the same Woods-Saxon mean field but with a different microscopic framework [26], the quasiparticle random-phase-approximation (QRPA), where only the excitation energy of the one-phonon wobbling band can be calculated microscopically. As for the force strengths of the interaction in Eq. (5), the so-called self-consistent value given in Ref. [1] is used for the particle-hole interaction,  $\chi$  (see Refs. [11,12] for details). For the particle-particle channels,  $g_\lambda^\tau$ , the monopole strength  $g_0^\tau$  is determined so that the self-consistently determined pairing parameter  $p_0^\tau = g_0^\tau \langle \hat{G}_{00}^\tau \rangle$  gives the proper average pairing gap in Eq. (9). The values of the latter are set equal to the even-odd mass difference for the ground state of even-even nucleus, where the deformation parameters are determined by the Woods-Saxon Strutinsky calculation of Ref. [27]. For the odd- $A$  or odd-odd nuclei, we use the average of the neighboring even-even nuclei. The quadrupole pairing parameter  $g_2^\tau$  is assumed to be proportional to  $g_0^\tau$  and the proportionality constant is chosen to be  $g_2^\tau/g_0^\tau = 1.980$ , which gives the correct  $2^+$  excitation energy of the ground-state rotational band in a typical rare-earth-metal nucleus  $^{164}\text{Er}$ . Thus, the Hamiltonian is not devised with the intention to describe the wobbling bands or the chiral doublet bands.

In most of the present investigation, we employ the Woods-Saxon mean field and the schematic interaction in Eq. (5). However, we also show some results of a more fully self-consistent approach, the angular-momentum projection from the mean field obtained by the self-consistent Hartree-Fock-Bogoliubov (HFB) method with the finite-range Gogny D1S interaction [28]. Recently, we have developed a computer code to perform such calculations, and it has been applied in our previous works [13–16]. For example, the ground-state rotational bands of the rare-earth-metal nuclei can be naturally reproduced [15,16]. The self-consistent cranking procedure is employed just like in Eq. (7), i.e., for  $\hat{H}' = \hat{H} - \omega_{\text{rot}} \cdot \hat{\mathbf{J}}$  with the Gogny interaction included in  $\hat{H}$ . The calculational method is exactly the same as in these references; in particular, the Slater approximation is used in order to prevent vanishing pairing correlation for protons in the ground state, although we can perform the calculation without this approximation. In contrast to the Woods-Saxon potential, the mean field is generated from the effective interaction in the Gogny-HFB approach and the self-consistent potential is nonlocal. Therefore, it is not easy to characterize the nuclear shape by the mean-field potential in this case: The shape of the mean field is specified by the density distribution. We use the deformation parameters defined, as

usual, by

$$\alpha_{\lambda,\mu}(\text{den}) \equiv \frac{4\pi \langle Q_{\lambda,\mu} \rangle}{3A \bar{R}^\lambda}, \quad \bar{R} \equiv \sqrt{\frac{5}{3A} \left\langle \sum_{i=1}^A (r^2)_i \right\rangle}, \quad (10)$$

where  $Q_{\lambda,\mu} = r^\lambda Y_{\lambda,\mu}$  is the mass  $\lambda$ -pole operator. In the same way, the amount of the pairing correlation is characterized by the average pairing gap,

$$\bar{\Delta} = \left[ - \sum_{a>b} \Delta_{ab} \kappa_{ab}^* \right] \left[ \sum_{a>0} \kappa_{aa}^* \right]^{-1},$$

$$\Delta_{ab} = \sum_{c>d} \bar{v}_{ab,cd} \kappa_{cd}, \quad (11)$$

where the quantities  $\bar{v}_{ab,cd}$  and  $\kappa_{ab}$  are the antisymmetrized matrix element of the two-body interaction and the abnormal pairing tensor, respectively [10]. In order to specify the intrinsic coordinate system of the mean field, we impose the constraints [29],  $\alpha_{21}(\text{den}) = \alpha_{2-1}(\text{den}) = 0$  and  $\alpha_{22}(\text{den}) = \alpha_{2-2}(\text{den})$ , and select the  $xyz$  coordinate axes to satisfy  $\langle x^2 \rangle \leq \langle y^2 \rangle \leq \langle z^2 \rangle$  corresponding to the Lund convention of the triaxiality parameter,  $0 \leq \gamma \leq 60^\circ$ .

In the present work, we mainly report the result for single mean field  $|\Phi\rangle$  with finite cranking frequencies [see Eq. (7)]. We employ the cranking procedure for changing the alignment and moments of inertia in our microscopic framework. It should, however, be emphasized that the cranking frequency is not an adjustable parameter from the theoretical point of view. It should be treated as a second generator coordinate combined with the angular-momentum projection

$$|\Psi_{M,\alpha}^I\rangle = \int \sum_K g_{K,\alpha}^I(\omega_{\text{rot}}) \hat{P}_{MK}^I |\Phi_{\text{cr}}(\omega_{\text{rot}})\rangle d\omega_{\text{rot}}, \quad (12)$$

which was originally proposed by Peierls and Thouless [30]. There are three cranking frequencies for triaxial cases. For simplicity, only one dimension is shown in Eq. (12). We have investigated this method, for the first time, for axially deformed cases in Refs. [15,16] with the Gogny interaction. The result is promising. We call it the angular-momentum-projected multicranked configuration-mixing method. Practically, several cranked mean-field states, e.g.,  $|\Phi_n\rangle = |\Phi(\omega_{\text{rot}}^{(n)})\rangle$ ,  $n = 1, 2, \dots, N_{\text{mf}}$ , are configuration mixed,

$$|\Psi_{M,\alpha}^I\rangle = \sum_{n=1}^{N_{\text{mf}}} \sum_K g_{K,\alpha}^I \hat{P}_{MK}^I |\Phi_n\rangle, \quad (13)$$

which is the discrete approximation of Eq. (12). This extended formulation is as straightforward as any generator-coordinate method (GCM), although the numerical task becomes much ( $N_{\text{mf}}^2$  times) heavier because the norm and Hamiltonian kernels should be evaluated between these several mean-field states. An application of this method will be discussed in Sec. III G.

### III. APPLICATION TO WOBBLING BAND

Wobbling motion is the quantized rotational motion of the rigid rotor, which is a characteristic collective motion for the triaxially deformed nucleus; see, e.g., Chaps. 4 and 5 of

Ref. [1]. After long-lasting experimental efforts, it has been first identified in  $^{163}\text{Lu}$  [6]. Nuclei in this region,  $Z \sim 70\text{--}72$  and  $N \sim 92\text{--}98$ , exhibit the so-called triaxial superdeformed (TSD) bands at high spin [31–33]. Therefore, we take the nucleus  $^{163}\text{Lu}$  as a typical example. The Nilsson-Strutinsky calculations predict deformation of  $\epsilon_2 \sim 0.4$  and  $\gamma \sim 20^\circ$  [36,43], where  $\epsilon_2$  is rather constant and the parameter  $\gamma$  only slightly increases as a function of angular momentum. By converting the deformation parameters to those of the Woods-Saxon potential in Sec. II, we use mainly  $\beta_2 = 0.42$ ,  $\beta_4 = 0.02$ , and  $\gamma = 18^\circ$  in the present work. The values of these parameters are the same as the previous work [25]. Since we do not aim at a detailed comparison with the experimental data, the pairing gaps for neutrons and protons are chosen to be constant,  $\Delta_n \approx \Delta_p \approx 0.5$  MeV, because the wobbling excitation is observed at high-spin states where the pairing correlations are considerably reduced. The calculations are performed within the isotropic harmonic oscillator basis. The basis states are included up to the maximum oscillator shells,  $N_{\text{osc}}^{\text{max}} = 12$ . As for the number of mesh points for the integration with respect to the Euler angles  $(\alpha, \beta, \gamma)$  in the angular-momentum-projector [10], we mainly use  $N_\alpha = N_\gamma = 42$ ,  $N_\beta = 80$ , but sometimes increase them up to  $N_\alpha = N_\gamma = 68$ ,  $N_\beta = 126$  to obtain the convergent result. For solving the Hill-Wheeler Eq. (2), small-norm solutions appear, which cause difficulties, see, e.g., Ref. [10], and should be discarded. We solve the equation several times with different norm cutoff values from  $10^{-13}$  to  $10^{-6}$ , i.e., the solutions that have smaller norm eigenvalues than these values are eliminated, and we adopt the reasonable result with the smallest possible value of the cutoff values. Here “reasonable” means that, for example, the spectrum as a function of the spin  $I$  is smooth enough.

We would like to mention that the self-consistently determined triaxiality parameter of the Nilsson potential  $\gamma(\text{Nils}) \sim 20^\circ$ , or of the Woods-Saxon potential  $\gamma(\text{WS}) \sim 18^\circ$ , corresponds to much smaller triaxial deformation  $\gamma(\text{den})$  of the density distribution for the mean-field state, which is defined by

$$\gamma(\text{den}) \equiv \tan^{-1} \left[ -\frac{\sqrt{2}\langle Q_{22} \rangle}{\langle Q_{20} \rangle} \right]; \quad (14)$$

see Ref. [34] for the precise definitions of these various  $\gamma$  parameters and discussion related to them. Namely,

$$\gamma(\text{Nils}) \sim 20^\circ, \quad \gamma(\text{WS}) \sim 18^\circ \Leftrightarrow \gamma(\text{den}) \sim 11\text{--}12^\circ, \quad (15)$$

for the considered large deformation of  $\epsilon_2 \sim 0.4$  or  $\beta_2 \sim 0.42$ . We have already confirmed in Ref. [35], which will be discussed later in Sec. III F, that the self-consistent HFB calculation with the Gogny D1S interaction also gives similar triaxial deformation,  $\gamma(\text{den}) \approx 11\text{--}12^\circ$ . With this relatively small value of the triaxial deformation, the out-of-band  $B(E2)$  for the excited TSD bands, which is a characteristic quantity to identify the wobbling motion, is considerably underestimated [25,34] (see also Ref. [36]). In Sec. III D, we will present also the results of angular-momentum-projection calculations with larger triaxial deformation than this self-consistently determined value.

### A. Longitudinal and transverse wobbling

Although the observed  $B(E2)$  values show the expected property for wobbling-phonon bands [6,37,38], the phonon excitation energy in the Lu isotopes decreases as a function of angular momentum, which is in contrast to the original prediction of the triaxial-rotor model [1]. Recently Frauendorf and Dönau gave an interpretation [20] for this decreasing behavior of the wobbling excitation energy within the simple triaxial particle-rotor model: The presence of the odd proton in the high- $j$   $i_{13/2}$  orbit can change the dependence of the excitation energy on the angular momentum. This was already pointed out in Ref. [39] but the interpretation was not appropriate (see also Refs. [7,8]). We briefly discuss the essence below, following Ref. [20].

Within the simple classical approximation, which is called “frozen alignment” approximation in Ref. [20], the total angular-momentum vector  $(J_x, J_y, J_z)$  with the aligned high- $j$  particle along the  $x$  axis of the deformed intrinsic body satisfies the equations

$$\begin{aligned} J_x^2 + J_y^2 + J_z^2 &= I(I+1), \\ \frac{(J_x - j)^2}{2\mathcal{J}_x} + \frac{J_y^2}{2\mathcal{J}_y} + \frac{J_z^2}{2\mathcal{J}_z} &= E, \end{aligned} \quad (16)$$

where the first one describes the conservation of angular momentum and the second is the rotor model energy. Here the quantities  $\mathcal{J}_x$ ,  $\mathcal{J}_y$ , and  $\mathcal{J}_z$  are the moments of inertia of the core nucleus in the intrinsic frame. For the fixed angular momentum  $I$ , energy  $E$ , and the alignment  $j$ , the angular-momentum vector moves along the trajectory given by the intersection of the sphere and the ellipsoid shifted by the amount  $j$  in the  $x$  direction as in Eq. (16). If the moments of inertia satisfy the condition that the alignment axis is the axis with the largest moment of inertia, i.e.,  $\mathcal{J}_x > \mathcal{J}_y, \mathcal{J}_z$ , the excitation energy of the quantized wobbling motion monotonically increases as a function of spin  $I$  in the same way as for the original rotor model without the aligned particle. In this case, the angular-momentum vector precesses always around the largest inertia axis  $x$ . However, if the inertia of the alignment axis is not the largest, for example,  $\mathcal{J}_y > \mathcal{J}_x > \mathcal{J}_z$ , it is shown that the excitation energy first increases and then decreases as a function of  $I$  [20]: The one-phonon excitation energy vanishes at the critical angular-momentum,

$$I_c = j \frac{\mathcal{J}_y}{\mathcal{J}_y - \mathcal{J}_x}, \quad (17)$$

which gives a transition from the principal-axis rotation (PAC) to the tilted-axis rotation (TAC) [40]. In this case, the angular-momentum vector precesses first around the alignment axis  $x$ , but then its direction moves to the largest inertia axis  $y$  when the spin increases; namely, a kind of transition of the main rotation axis from one of the principal axes to the other occurs. An instructive argument for the mechanism of this transition can be found in Sec. 3.8.6 of Ref. [8]. It will be discussed that the spin dependence of the excitation energies reflects this change of the direction of the angular-momentum vector in the intrinsic frame. Frauendorf-Dönau called these two different cases longitudinal and transverse wobbling, respectively, in

Ref. [20] to indicate the different center of the intersection trajectory of Eq. (16) in each case. We will show that the simple picture is indeed realized in the fully microscopic calculation of angular-momentum projection.

### B. Wobbling motion in even-even core nucleus

In order to study the wobbling spectrum, we first investigate the “core” nucleus, i.e., the even-even neighbor  $^{162}\text{Yb}$  of the odd-proton nucleus  $^{163}\text{Lu}$ . A brief research of the wobbling motion in the even-even nucleus  $^{164}\text{Er}$  using the angular-momentum-projection approach has been recently performed in Ref. [14] in relation to the study of the  $\gamma$  vibrational band. In fact, it is expected [41] that the high-spin extension of the  $\gamma$  vibrational band changes its character to wobbling motion. In contrast to Ref. [14], where the Gogny interaction has been employed, we use in Sec. II the Woods-Saxon mean field and the schematic interaction consistent with it. The mean-field parameters, the deformations and the average pairing gaps, are simply chosen to be the same as in  $^{163}\text{Lu}$ , which are explained in the beginning of this section. It is shown that the result is not very different from that in  $^{164}\text{Er}$ . It should, however, be noted that this analysis is not realistic for the nucleus  $^{162}\text{Yb}$ : The TSD state appears in the yrast region by occupying the Nilsson orbits originating from the proton  $i_{13/2}$  state, which is not occupied in the Yb isotopes in normal situations. So the TSD states of the  $^{162}\text{Yb}$  in the present work has just a meaning of the possible core state of the TSD bands of  $^{163}\text{Lu}$ .

As mentioned in the previous subsection, Sec. III A, the values of the moments of inertia of the core nucleus are very important to interpret the wobbling excitation energy [see, e.g., Eq. (16)]. In the fully microscopic framework of the present work, the moments of inertia are not introduced explicitly but they should be extracted from the resultant spectrum of calculation. However, there is no unique way to relate the calculated energy spectrum to the three moments of inertia. We show the cranking moments of inertia [10] in Fig. 1 as functions of the  $\gamma$  deformation. They are calculated as  $\mathcal{J}_i = \lim_{\omega_i \rightarrow 0} \langle J_i \rangle / \omega_i$ , where  $\omega_i$  is the cranking frequency about the  $i$ th axis ( $i = x, y, z$ ) in Eq. (7). In Eq. (15), the values of the triaxiality parameter specifying the Woods-Saxon potential shape  $\gamma(\text{WS})$  and that of the density distribution  $\gamma(\text{den})$  are considerably different, so that the inertias as functions of  $\gamma(\text{WS})$  are shown in Fig. 1(a), while those as functions of  $\gamma(\text{den})$  are shown in Fig. 1(b). The moments of inertia calculated with larger pairing gaps,  $\Delta_n = \Delta_p = 1.0$  MeV, which roughly correspond to the ground-state values, are also shown in Fig. 1(c). For reference, the macroscopic irrotational-flow inertias are also included in Fig. 1(d). It can be seen that the largest inertia is that of the medium axis, i.e., the one of the  $y$  axis for  $0 < \gamma < 60^\circ$ , as in the case of irrotational flow. The calculated moments of inertia as functions of  $\gamma(\text{den})$  resemble more the irrotational-flow inertias than those as functions of  $\gamma(\text{WS})$ , which is usually used to specify the triaxiality of the Woods-Saxon potential. The  $\gamma$  parameter of the irrotational moments of inertia is naturally interpreted as that of the density distribution. However, the relative values of three calculated moments of inertia are considerably different from those of irrotational flow. For example, at  $\gamma = 30^\circ$ , the irrotational flow  $\mathcal{J}_y$  is four times larger than

$\mathcal{J}_x = \mathcal{J}_z$ , while the microscopically calculated  $\mathcal{J}_y$  is only about two times larger. Moreover, the symmetry with respect to  $\gamma = 30^\circ$  is not present in the microscopic cranking moments of inertia. It is known that the values of the cranking inertia are generally different for the prolate and oblate shapes even with the same  $\beta_2$  deformation. The “unnatural” bump-like behavior of the calculated inertia  $\mathcal{J}_x$  at  $\gamma(\text{WS}) \approx 24^\circ$  ( $\gamma(\text{den}) \approx 16^\circ$ ) is due to a sharp level crossing of the neutron single-particle Routhians at the Fermi surface (see, e.g., Fig. 1 of Ref. [25]). Thus, the moments of inertia  $\mathcal{J}_x$  and  $\mathcal{J}_y$  at the triaxiality parameter in Eq. (15) are comparable and satisfy  $\mathcal{J}_y \gtrsim \mathcal{J}_x \gg \mathcal{J}_z$ . An estimated value for the critical angular momentum in Eq. (17) at  $\gamma(\text{WS}) = 18^\circ$  is rather large,  $I_c \approx 50.1$ , for  $j = 13/2$ . It should be noticed that these values of the inertias at the triaxiality in Eq. (15) are very similar to those in Ref. [20].

Now we show in Fig. 2 the spectrum calculated by angular-momentum projection from the Woods-Saxon mean field with the deformation parameters specified in the beginning of this section, especially the  $\gamma$  deformation parameter in Eq. (15). No cranking is performed for the mean-field state in the upper panels. The lowest energy is chosen to be the energy origin ( $E(I=0) = 0$ ), and the rigid-rotor reference energy  $0.007 I(I+1)$  MeV is subtracted here and in the following calculations. The value 0.007 roughly corresponds to the one obtained by the moment of inertia of the observed TSD1 band in  $^{163}\text{Lu}$ . As is clearly seen in the figure, the spectrum shows the multiple-band structure characteristic for the wobbling motion. Note that only one rotational band appears if the mean field is axially symmetric. In the right panels of the figure, the excitation energies of the lowest bands are depicted as functions of the angular momentum. The excitation energies of the excited bands increase just as they are expected for even-even nuclei [1]. The first excited band has odd spin and the second excited band has even spin, etc. The signature of the excited band changes alternatively. At the low-spin states, the first and the second excited bands are almost degenerate and compose the  $\gamma$ -band-like structure,  $2^+, 3^+, 4^+, \dots$ , but the degeneracy is lifted after  $I \gtrsim 10$ . Note that we always refer the spin values  $I$  in units of  $\hbar$ . It should be mentioned, however, that the calculated moment of inertia for the yrast band is rather small, about  $\mathcal{J}^{(1)} \approx 32 \hbar^2/\text{MeV}$  at  $I \approx 20$ , where the first moment of inertia is defined by

$$\mathcal{J}^{(1)}(I) = \frac{(2I+1)\hbar^2}{E(I+1) - E(I-1)}. \quad (18)$$

Compared with moment of inertia obtained for the observed TSD1 band of  $^{163}\text{Lu}$ , the calculated value is less than half. It has been pointed out that it is important to include the time-odd components into the wave function to obtain the correct moment of inertia. The easiest way to incorporate them is to use small frequency cranking. We called it “infinitesimal cranking” in Ref. [14], where it has been shown that the excitation energy of the  $\gamma$  vibration and the moments of inertia both of the ground-state band and of the  $\gamma$  band are improved. We show the result of the projection from the infinitesimally cranked mean field with  $\omega_x = \omega_y = \omega_z = 0.01$  MeV/ $\hbar$  in the lower panels in Fig. 2. Here the small cranking frequency 10 keV is chosen to include the time-odd contributions without the higher order

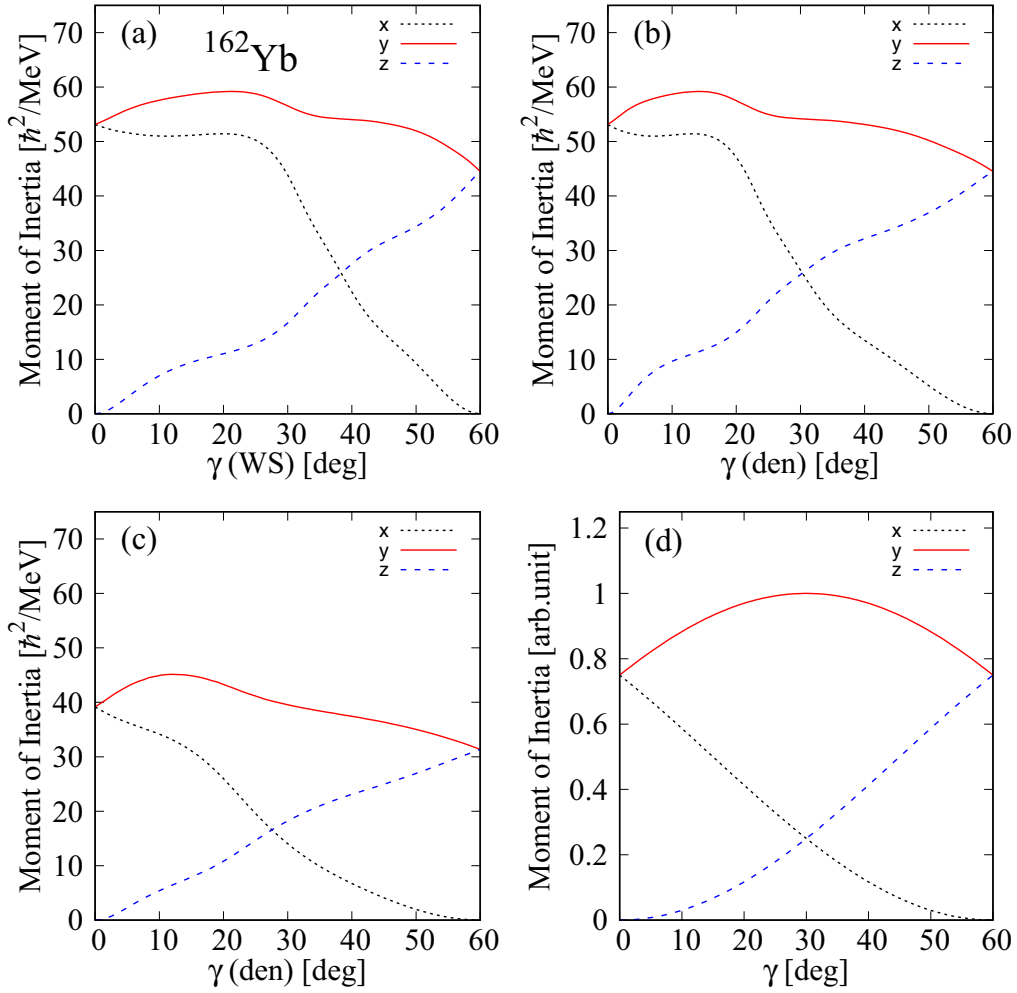


FIG. 1. Cranking moments of inertia of the three intrinsic axes,  $x$ ,  $y$ , and  $z$ , which are the short, medium, and long axes and denoted by dotted, solid, and dashed lines, respectively, as functions of the triaxiality parameter  $\gamma$  for the even-even core nucleus  $^{162}\text{Yb}$  of  $^{163}\text{Lu}$ . The deformation parameters  $\beta_2 = 0.42, \beta_4 = 0.02$  and the pairing gaps  $\Delta_n = \Delta_p = 0.5$  MeV are employed for the upper panels, (a) and (b), and the larger pairing gaps  $\Delta_n = \Delta_p = 1.0$  MeV for panel (c). The  $\gamma$  parameter of the Woods-Saxon potential is utilized in panel (a) and that of the density distribution, Eq. (14), in panels (b) and (c). Panel (d) shows the irrotational-flow moments of inertia in arbitrary units.

effects. The result is independent of the particular choice of this value (see Ref. [14] for the proof). Comparing the upper and lower panels of Fig. 2, the moment of inertia for the yrast band is increased by infinitesimal cranking. However, the value of  $\mathcal{J}^{(1)} \approx 44 \hbar^2/\text{MeV}$  at  $I \approx 20$ , is still considerably smaller than experimental one even if one considers the fact that the effect of alignment is present for  $\mathcal{J}^{(1)}$  of  $^{163}\text{Lu}$ . Therefore, we are mainly concerned about the excitation energies from the yrast band. The effect of infinitesimal cranking is also large for the excitation energies of the multiple wobbling bands, and the energies of the first and second excited bands start to split at lower spin values. It is, however, noted that the basic feature of the multiple wobbling bands are the same; e.g., the excitation energies increase as functions of spin.

In order to study the dynamical motion of the angular-momentum vector, we consider the expectation values of the angular-momentum vector in the body-fixed frame specified by the mean field, from which the projection is performed. The expectation values of the components of the angular-

momentum vector in the intrinsic frame are not well-defined quantities for the angular-momentum projected wave function in Eq. (1). We follow the previous work [14] and define them for the projected eigenstate  $\alpha$  in the following way,

$$((J_i^2))_\alpha \equiv \sum_{KK'} f_{K,\alpha}^{I*} \langle IK | J_i^2 | IK' \rangle f_{K',\alpha}^I, \quad (19)$$

where the index  $i = x, y, z$  denotes the axis specified by the deformed intrinsic mean-field wave function  $|\Phi\rangle$ , and the amplitudes ( $f_{K,\alpha}^I$ ) are the properly normalized ones in Eq. (4) obtained by the projection calculation. Needless to say, the purely algebraic quantity  $\langle IK | J_i^2 | IK' \rangle$ , e.g.,  $\langle IK | J_z^2 | IK' \rangle = \delta_{KK'} K^2$ , should be calculated in the intrinsic frame with  $[J_x, J_y] = -i\hbar J_z$ , etc. The microscopic geometrical information is contained in the amplitudes  $f_{K,\alpha}^I$ . A more microscopic definition by using the mean-field wave function with the projection operator can be introduced, which is shown to be consistent with the definition above; see the discussion in the

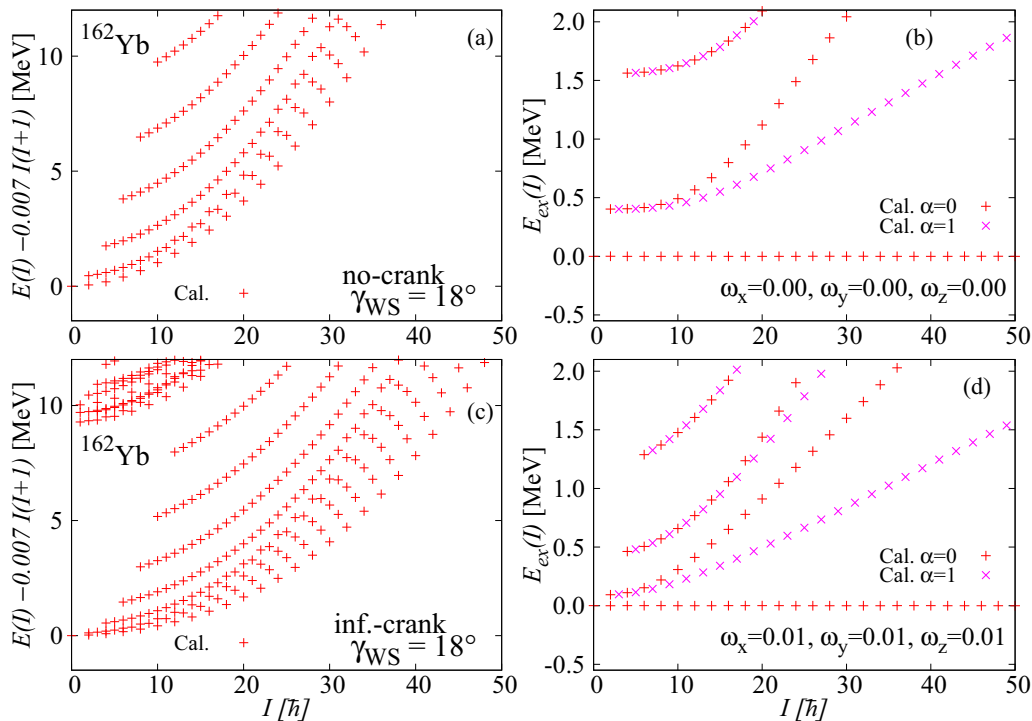


FIG. 2. The calculated spectrum (left panels) and the relative excitation energies (right panels) for  $^{162}\text{Yb}$  obtained by the angular-momentum-projection method. The rigid-rotor reference energy  $0.007 I(I+1)$  MeV is subtracted in the left panels. The upper panels are the result of projection from the noncranked mean field, while the lower panels are from the infinitesimally cranked mean field, with  $\omega_x = \omega_y = \omega_z = 0.01$  MeV/ $\hbar$ .

appendix of Ref. [14]. We show the result for the infinitesimal cranking case in Fig. 3, which corresponds to the lower panels of Fig. 2. The result for the no-cranking case is very similar and is not shown. As can be seen from the behavior of the three moments of inertia in Fig. 1, the angular-momentum vector precesses mainly about the largest inertia axis, i.e., the medium ( $y$ ) axis, and tilts slightly to the second-largest inertia axis, i.e., the short ( $x$ ) axis, for both the yrast and the first excited bands. For the first excited band, the vector more tilts to the direction of the  $x$  axis, with essentially no components along the smallest inertia axis, i.e., the long ( $z$ ) axis, for both the yrast and the

first excited bands. This behavior of the expectation values of the angular-momentum vector in the body-fixed frame are very similar to the case of  $^{164}\text{Er}$  studied in the previous work [14].

We study the wobbling spectrum obtained by the angular-momentum projection from the cranked mean field. In the upper and lower panels of Fig. 4, we show the excitation energies and the expectation values of angular-momentum vector for the case with  $\omega_x = 0.30$  MeV/ $\hbar$ ,  $\omega_y = \omega_z = 0.01$  MeV/ $\hbar$  and with  $\omega_x = 0.40$  MeV/ $\hbar$ ,  $\omega_y = \omega_z = 0.01$  MeV/ $\hbar$ , respectively. For the case with  $\omega_x = 0.30$  MeV/ $\hbar$ , there is

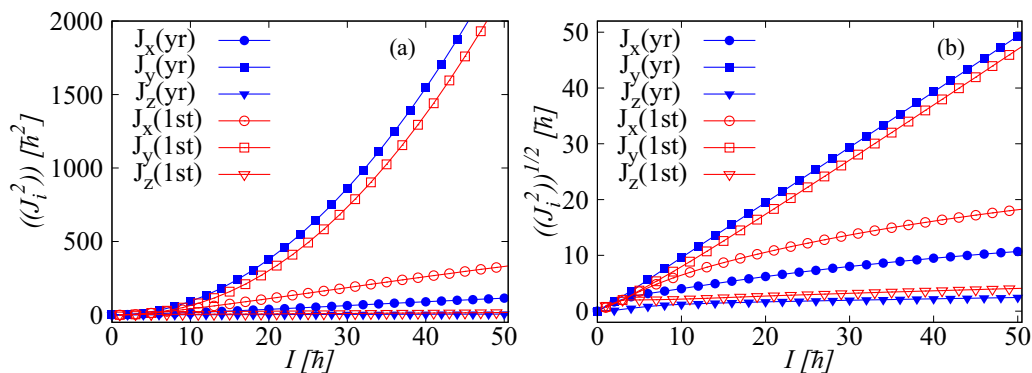


FIG. 3. The calculated behavior of the angular-momentum vector in the body-fixed frame for the yrast and the first excited bands in  $^{162}\text{Yb}$ . Here the mean field is infinitesimally cranked with  $\omega_x = \omega_y = \omega_z = 0.01$  MeV/ $\hbar$  corresponding to the lower panels of Fig. 2. The left panel shows the expectation values of the components of squared angular-momentum operator defined by Eq. (19), while the right panel shows the square root of them.

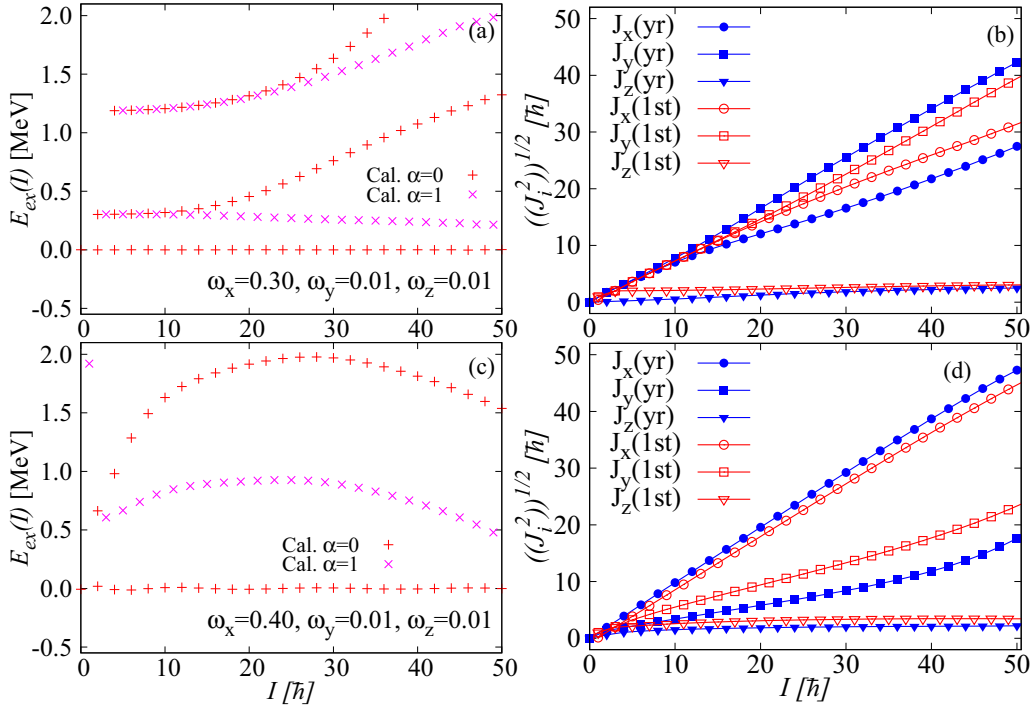


FIG. 4. The calculated excitation energy (left panels) and the expectation values of the angular-momentum vector (right panels) in  $^{162}\text{Yb}$  calculated by the projection from the cranked mean field with the frequencies  $\omega_x = 0.30$ ,  $\omega_y = \omega_z = 0.01$  MeV/ $\hbar$  (upper panels) and those with the frequencies  $\omega_x = 0.40$ ,  $\omega_y = \omega_z = 0.01$  MeV/ $\hbar$  (lower panels).

still no sharp alignment in the cranked wave function, but the mean-field contains a considerable amount of collective rotational angular momentum of  $\langle J_x \rangle \approx 16.5 \hbar$ . Therefore, the components of the angular-momentum vector for the  $x$  and  $y$  axes are comparable and then the excitation energy of the first excited band does not increase but is almost constant as a function of spin. Just after  $\omega_x = 0.30$  MeV/ $\hbar$ , the two  $i_{13/2}$  proton quasiparticles align their angular momenta along the  $x$  axis (see, e.g., the quasiparticle energy diagram, Fig. 2 in Ref. [25]), and the mean-field expectation value jumps to  $\langle J_x \rangle \approx 33 \hbar$  for  $\omega_x = 0.40$  MeV/ $\hbar$  (the collective angular momentum also contributes when increasing the rotational frequency from  $\omega_x = 0.30$  to  $0.40$  MeV/ $\hbar$ ). Thus, the expectation value of the angular-momentum vector has the largest component for the  $x$  axis in this case, as is seen in the lower right panel of Fig. 4, and the behavior of the excitation energy completely changes from that of the lower cranking frequencies in the upper panel of Fig. 4 or in Fig. 2. Apparently, in this case, the excitation energy first increases and then gradually decreases as a function of spin, which resembles the behavior of the transverse wobbling. However, the whole spectrum looks also very different from those in the case of the noncranked or of the infinitesimally cranked mean field in Fig. 2, as it is displayed in Fig. 5, where the lowest state is not  $I = 0^+$  state but  $I = 16^+$  state, because of the large aligned angular momentum along the short ( $x$ ) axis. In this way, the effect of alignment changes the dynamical behavior of the angular-momentum vector in the body-fixed frame, which seems to be reflected to the wobbling-phonon excitation energy. We will confirm this interesting relation in more detail in the following for the odd nucleus  $^{163}\text{Lu}$ .

### C. Wobbling motion in odd nucleus $^{163}\text{Lu}$

For the study of the wobbling motion in the odd nucleus  $^{163}\text{Lu}$ , it is important to recognize which orbit the odd proton occupies. With the deformation  $(\beta_2, \beta_4) = (0.42, 0.02)$  and the triaxiality parameter in Eq. (15), the positive-parity proton orbit at the Fermi surface originates from the high- $j$   $i_{13/2}$  particle, which strongly favors aligning its angular momentum along the short axis, i.e., the  $x$  axis for  $0 < \gamma < 60^\circ$ . In fact, the occupation of this orbit strongly polarizes nucleus to have sizable positive- $\gamma$  triaxial deformation (see, e.g., Refs. [31,32,43]). Considering that the even-even core nucleus has the moments

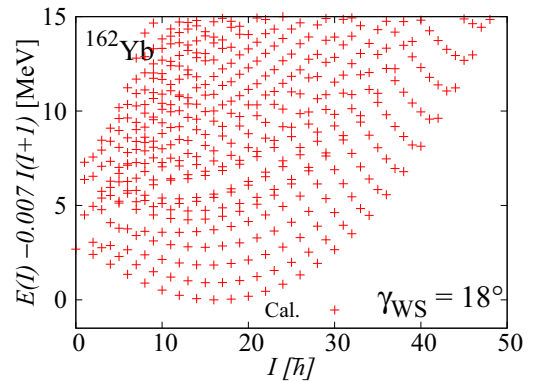


FIG. 5. The spectrum of the angular-momentum projection obtained from the cranked mean field with the frequencies  $\omega_x = 0.40$ ,  $\omega_y = \omega_z = 0.01$  MeV/ $\hbar$  in  $^{162}\text{Yb}$ , corresponding to the lower panels of Fig. 4.



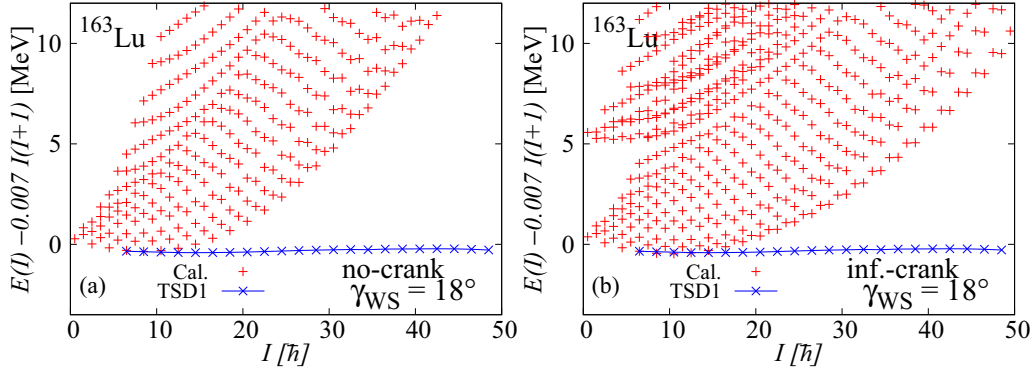


FIG. 6. Wobbling spectrum for  $^{163}\text{Lu}$  calculated by the angular-momentum-projection method from the noncranked mean field (left panel) and from the infinitesimally cranked mean field with the frequencies  $\omega_x = \omega_y = \omega_z = 0.01 \text{ MeV}/\hbar$  (right panel). The rigid-rotor reference energy  $0.007 I(I + 1) \text{ MeV}$  is subtracted for both the calculated and experimental energies. The energy of the experimental TSD1 [37] is also included in each panel.

of inertia satisfying  $\mathcal{J}_y \gtrsim \mathcal{J}_x \gg \mathcal{J}_z$  (see Fig. 1), the condition for the transverse wobbling discussed in Sec. III A is satisfied.

To construct the mean-field state with odd proton number, one has to block a proton quasiparticle [10]. When the cranking procedure is employed, there is no ambiguity because the cranked quasiparticle energies are nondegenerate, and the lowest proton quasiparticle state is blocked. In the case of no cranking, however, there is the Kramers twofold degeneracy. The mean-field state is ambiguous because any linear combinations of the two degenerate quasiparticle states can be taken to construct it. It should be stressed that this ambiguity of the mean field with the odd particle number causes no problem for angular-momentum projection; i.e., the projected energy is unique. This is because the two independent quasiparticle states are transformed by the  $\pi$  rotation around one of the coordinate axes into each other, and therefore they produce exactly the same spectrum by the angular-momentum projection (cf., the identity,  $\hat{P}_{MK}^I \hat{R} |\Phi\rangle = \hat{P}_{MK}^I |\Phi\rangle$ , where  $\hat{R}$  is a rotational operator at any Euler angle). We have numerically confirmed this fact.

We first show in Fig. 6 the calculated spectrum of angular-momentum projection from the noncranked mean field (left panel) and from the infinitesimally cranked mean field with  $\omega_x = \omega_y = \omega_z = 0.01 \text{ MeV}/\hbar$  (right panel), where the experimental energy of the TSD1 band is also included. The rigid-rotor reference energy  $0.007 I(I + 1) \text{ MeV}$  is subtracted from both the calculated and experimental energies. The lowest energy state, whose energy is chosen to be the origin (zero energy), has  $I^\pi = 9/2^+$  for no cranking (left panel), while it has  $I^\pi = 13/2^+$  for infinitesimal cranking (right panel). The experimental data for the lowest band, i.e., the TSD1 band, is also shown, in which the lowest observed state has  $I^\pi = 13/2^+$ . It is confirmed that the lowest (yrast) band has the signature  $\alpha = +1/2$ , the first excited band  $\alpha = -1/2$ , etc.; the signatures of the excited bands change alternatively as is expected for the wobbling motion with a  $\pi i_{13/2}$  odd nucleon. In both cases, the multiple-band structure expected for the wobbling motion appears naturally. However, the calculated moments of inertia of the wobbling bands are considerably underestimated compared with those of the experimental TSD1

band: The calculated  $\mathcal{J}^{(1)}$  in Eq. (18) for the noncranked mean field is about  $38 \hbar^2/\text{MeV}$  at  $I \approx 20$ , in contrast to the experimentally measured value about  $69 \hbar^2/\text{MeV}$ . Infinitesimal cranking improves the situation,  $\mathcal{J}^{(1)} \approx 46 \hbar^2/\text{MeV}$  at  $I \approx 20$ , though not enough, which is similar to the results of the even-even core nucleus  $^{162}\text{Yb}$ . Some improvement for the microscopic Hamiltonian and/or some adjustment of the interaction strengths may be necessary to reproduce the experimental spectrum, which is out of the scope of the present investigation. Therefore, we mainly concentrate on the excitation energies of the wobbling-phonon bands.

It may be worth mentioning that an extra multiple-band structure appears at higher excitation energy  $\gtrsim 5 \text{ MeV}$ , when infinitesimally cranked in the right panel of Fig. 6. It is interpreted as wobbling bands excited on some of higher quasiparticle configurations that are included by infinitesimal cranking. A similar structure at higher excitation energy  $\gtrsim 9 \text{ MeV}$  is also seen for  $^{162}\text{Yb}$  in the lower-left panel in Fig. 2. Such excited wobbling structures appear in the result of projection from cranked mean fields, but how many they are and what excitation energies they have depends on each case.

Figure 7 displays the calculated excitation energies and the expectation values of the angular-momentum vector in the intrinsic frame for the cases with the noncranked and the infinitesimally cranked mean fields in the upper and lower panels, respectively. The experimental excitation energies are also included in the left panels. It can be seen from the left panels that the characteristic features of the transverse wobbling are realized in these calculations. Namely, the excitation energy of the one-phonon wobbling band first increase and then decrease as spin increases, and it vanishes at the critical angular momentum,  $I_c \approx 36$  ( $I_c \approx 20$ ), in the upper-left (lower-left) panel of Fig. 7. The excitation energy does not exactly vanish but the energies of the lowest and the first excited bands repel with each other, i.e., there is a virtual crossing. Comparing the upper and lower panels in Fig. 7, the infinitesimal cranking reduces the excitation energies and therefore the critical angular momentum of the vanishing one-phonon wobbling excitation energy becomes lower. Moreover, the main component of the angular-momentum vector in the intrinsic frame is along the

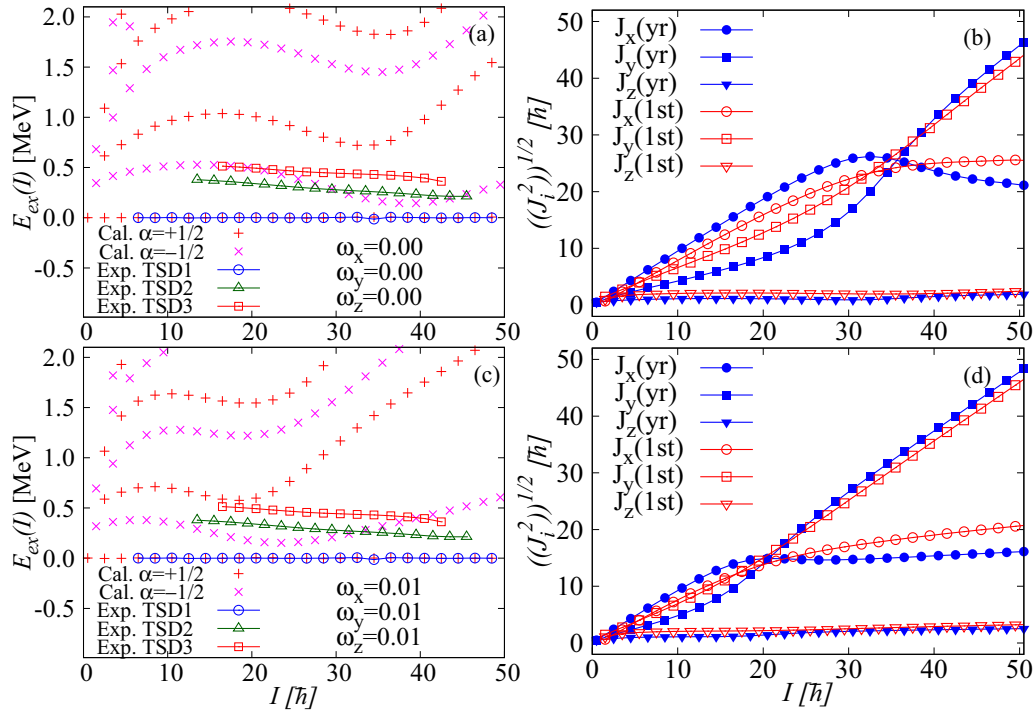


FIG. 7. The calculated excitation energy (left panels) and the expectation values of the angular-momentum vector (right panels) in  $^{163}\text{Lu}$  calculated by the projection from the noncranked mean field (upper panels) and those from the infinitesimally cranked mean field with  $\omega_x = \omega_y = \omega_z = 0.01 \text{ MeV}/\hbar$  (lower panels). The experimental excitation energies of TSD1, TSD2, and TSD3 [37] are also included in the left panels.

alignment axis (short axis),  $x$  axis, at low spins, and it changes to be along the largest inertia axis,  $y$  axis, at high spins. As expected, the spin value, where the main component exchanges from that of  $x$  axis to that of  $y$  axis,  $((J_x^2)^{1/2} \approx ((J_y^2)^{1/2})$ , almost corresponds to the critical angular momentum. Note that the collective rotation takes place around the short ( $x$ ) axis at low-spin states induced by the alignment of  $\pi i_{13/2}$  particle, even if the core moments of inertia satisfy  $\mathcal{J}_x \lesssim \mathcal{J}_y$  (see Fig. 1): The maximum values of  $((J_x^2)^{1/2})$  are about 27 and 15 in the upper and lower panels of Fig. 7, respectively, which are much larger than the maximum alignment of one  $i_{13/2}$  quasiparticle,  $j = 13/2$ . This behavior of the angular-momentum vector is consistent with transverse wobbling in the classical model in Eq. (16) (see also the discussion in Ref. [8]).

This correspondence between the wobbling-phonon excitation energy and the behavior of the angular-momentum vector in the intrinsic frame seems to be rather general. Figure 8 shows the result of calculation using cranked mean fields with higher rotational frequencies  $\omega_x = 0.20$  and  $0.40 \text{ MeV}/\hbar$  in the upper and lower panels, respectively, on top of the infinitesimal cranking. As it is seen, the wobbling-phonon excitation energy increases by increasing the rotational frequency around the alignment axis ( $x$  axis), and the critical angular momentum of the vanishing one-phonon energy becomes higher. This is consistent with the macroscopic particle-rotor model of the transverse wobbling referred to in Sec. III A; the higher cranking frequency  $\omega_x$  effectively increases the alignment and/or the moment of inertia about the  $x$  axis, so that the critical angular momentum  $I_c = j(1 - \mathcal{J}_x/\mathcal{J}_y)^{-1}$  delays. Compared

with the experimental data, the one-phonon excitation energy decreases too quickly as a function of spin. Moreover, the two-phonon excitation energy is almost double of the one-phonon energy, which is too large in comparison with the data. The experimental TSD3 excitation energy is much smaller than the double of the TSD2 excitation energy. Thus, our results of the projection calculation are not very successful in reproducing the experimental spectrum.

In this way it is demonstrated that the wobbling excitation energy is sensitive to the dynamics of the angular-momentum vector in the intrinsic frame, which is controlled by cranking of the mean field. The decrease of the one-phonon energy is related to the change of the main component of the angular-momentum vector, i.e., the decrease of  $((J_x^2)^{1/2} - ((J_y^2)^{1/2})$ , which changes sign near the critical angular momentum of the vanishing excitation energy. We show two more examples, where the cranking with the frequency  $0.2 \text{ MeV}/\hbar$  is performed around the largest and smallest inertia axes ( $y$  and  $z$  axes) in the upper and lower panels of Fig. 9, respectively, on top of the infinitesimal cranking. As it is seen, the result of the cranking around the largest inertia axis in the upper panels is not very different from that of the simple infinitesimal cranking in the lower panels of Fig. 7. Although the cranking around  $y$  axis increases  $((J_y^2)^{1/2})$ , the frequency,  $\omega_y = 0.2 \text{ MeV}/\hbar$ , is not large enough to change the alignment pattern: The main rotation axis is still the short axis at low spins, and only the critical angular momentum becomes smaller, which is also consistent with the simple model estimate,  $I_c = j(1 - \mathcal{J}_x/\mathcal{J}_y)^{-1}$ . The excitation energies of the wobbling motion look like those of

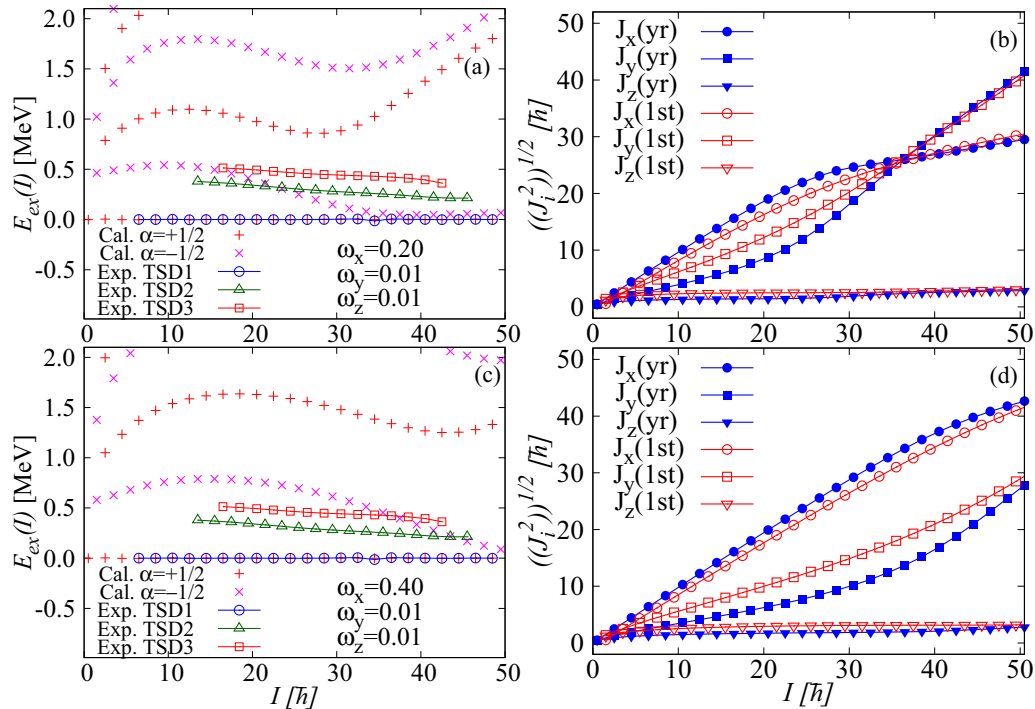


FIG. 8. The calculated excitation energy (left panels) and the expectation values of the angular-momentum vector (right panels) in  $^{163}\text{Lu}$  calculated by the projection from the cranked mean field with the frequencies  $\omega_x = 0.20$ ,  $\omega_y = \omega_z = 0.01$  MeV/ $\hbar$  (upper panels), and those with the frequencies  $\omega_x = 0.40$ ,  $\omega_y = \omega_z = 0.01$  MeV/ $\hbar$  (lower panels).

the longitudinal wobbling at spins higher than the critical one. On the other hand, cranking around the long axis in the lower panels of Fig. 9 changes the result of projection in a different way compared with the lower panels of Fig. 7. The critical angular momentum is increased but the excitation energies of the wobbling phonon become considerably smaller, and the multiple-band structure is more clearly exhibited. The critical angular momentum is similar to the result of cranking around the intermediate-inertia axis ( $x$  axis) in the upper panels of Fig. 8, while the wobbling excitation energies are considerably smaller. In the case of the  $z$  axis cranking, the component of angular-momentum along the largest-inertia axis ( $y$  axis) is more reduced at lower spins as it can be seen by comparing the lower panels of Figs. 9 and the upper panels of Figs. 8. It is interesting that such a difference between the expectation values of the angular-momentum vector in the intrinsic frame is clearly reflected in the wobbling excitation energies.

It is demonstrated that the cranking of the mean field around the  $x$  axis increases the wobbling excitation energies while the cranking around the  $z$  axis reduces them. However, the cranking procedure also change the slope of the rotational spectrum, i.e., the moment of inertia of the rotational band. We compare the spectrum calculated with cranking around the  $x$  axis and the  $z$  axis in Fig. 10. The cranking around the  $z$  axis makes the moment of inertia of the TSD1 band considerably smaller,  $\mathcal{J}^{(1)} \approx 38\hbar^2/\text{MeV}$  at  $I \approx 20$ , as it is displayed in the right panel in comparison with the cranking around the  $x$  axis in the left panel, in this case,  $\mathcal{J}^{(1)} \approx 53\hbar^2/\text{MeV}$  at  $I \approx 20$ . Therefore, the cranking only around the long axis ( $z$  axis) is not favorable for high-spin states.

In comparison with the experimental data, all the results presented for the wobbling excitation energies, Figs. 7–9 are not satisfactory. Especially, the critical angular-momentum,  $I_c$ , where the one-wobbling-phonon excitation energy vanishes and the main component of angular-momentum vector in the intrinsic frame changes from that of the alignment axis ( $x$ ) to the largest inertia axis ( $y$ ), is too small. The experimental excitation energy does not vanish in the observed range of angular momentum, and therefore  $I_c > 91/2$  at least. The calculated result presented so far, which satisfies this inequality, is the case of the high-frequency cranking around the  $x$  axis with  $\omega_x = 0.4$ ,  $\omega_y = \omega_z = 0.01$  MeV/ $\hbar$  displayed in the lower panels of Fig. 8; the wobbling excitation energy is, however, too high in this case. In order to study the properties of the electromagnetic transition probabilities, the intrinsic nuclear shape, which is kept constant in the present work, and the geometry of the angular-momentum vector in the intrinsic frame are important. Therefore, we slightly change the cranking frequencies and make the critical angular momentum higher, still keeping the one-wobbling-phonon excitation energy relatively low as in the experimental data: Figure 11 depicts the wobbling-excitation energies and the expectation values of the angular-momentum vector for the cranked mean field with the frequencies,  $\omega_x = 0.20$ ,  $\omega_y = 0.0$ ,  $\omega_z = 0.01$  MeV/ $\hbar$ . The agreement of the excitation energy is much better, although that of the two-phonon-wobbling band is still too high. We found it difficult to obtain such low excitation energy for the two-phonon wobbling band in the present calculation.

With this choice of the cranking frequencies and the excitation spectrum of Fig. 11, the calculated  $I \rightarrow I - 2$  in-band  $E2$

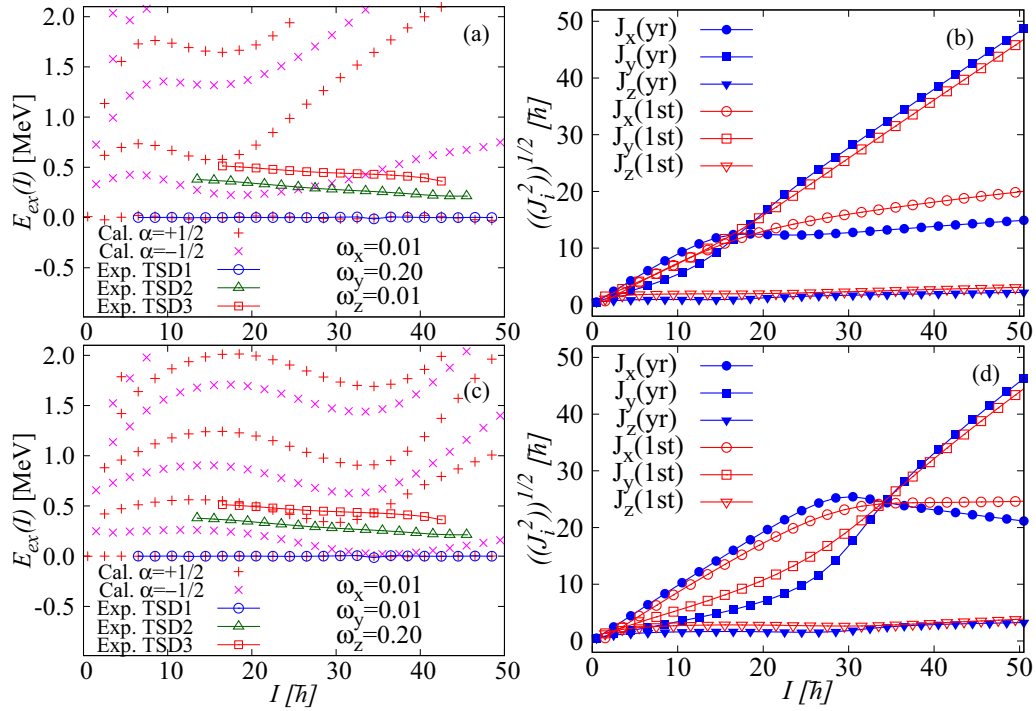


FIG. 9. The calculated excitation energy (left panels) and the expectation values of the angular-momentum vector (right panels) in  $^{163}\text{Lu}$  calculated by the projection from the cranked mean-field with the frequencies  $\omega_x = 0.01$ ,  $\omega_y = 0.20$ ,  $\omega_z = 0.01$  MeV/ $\hbar$  (upper panels), and those with the frequencies  $\omega_x = \omega_y = 0.01$ ,  $\omega_z = 0.20$  MeV/ $\hbar$  (lower panels).

transition probabilities and the ratios of the  $I \rightarrow I \pm 1$  out-of-band to in-band  $B(E2)$  are compared with the experimental data in Fig. 12. As seen, the in-band  $B(E2)$  values are almost constant and agree with the experimental value at low spin,  $I \approx 20$ . However, the measured values decrease as a function of spin in contrast to the calculation. As for the out-of-band  $B(E2)$  values from TSD2 to TSD1, there are two possible transitions with  $I \rightarrow I \pm 1$ . The rotor model predicts [1] that the  $I \rightarrow I - 1$  transitions are much stronger for the so-called positive- $\gamma$  rotation (see below for explanation) in agreement with the projection calculation. Only the  $I \rightarrow I - 1$  transitions are measured in the experiment, which is considered to be consistent with the rotor model prediction. The calculated

$I \rightarrow I - 1$   $B(E2)_{\text{out}}/B(E2)_{\text{in}}$  ratio from TSD2 to TSD1 at low spin,  $I \approx 15$ , is also comparable with the experimentally measured value, but the calculated ratios decrease as functions of spin, which is in agreement with the rotor model prediction because of the  $1/I$  factor of the relevant squared Clebsch-Gordan coefficients [1]. In contrast, the measured values are almost constant or even increase at the highest spins observed. The observed  $B(E2)_{\text{out}}/B(E2)_{\text{in}}$  ratio from TSD3 to TSD2 is larger by almost a factor of 2 than that from TSD2 to TSD1, but the calculated values for both transitions are considerably smaller at higher spins,  $I \gtrsim 22$ . As for the  $B(M1)$  transitions, the calculated out-of-band  $B(M1)$  to in-band  $B(E2)$  ratio is displayed in Fig. 13. The out-of-band  $B(M1)$  transitions with

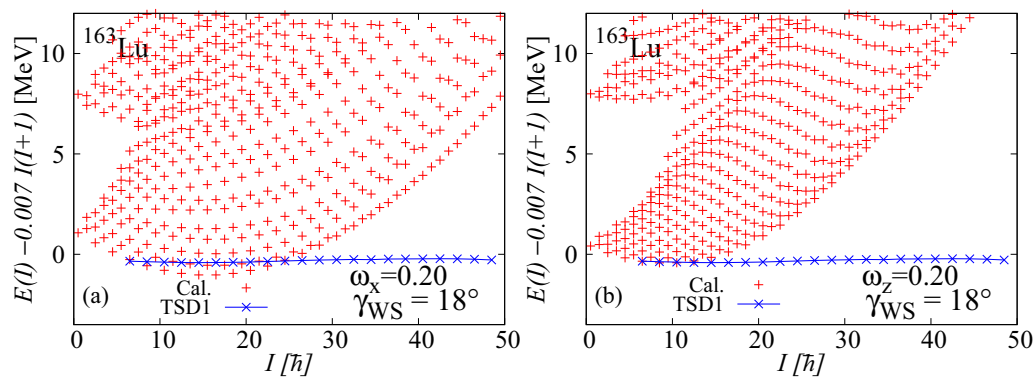


FIG. 10. Wobbling spectrum for  $^{163}\text{Lu}$  calculated by the projection from the cranked mean field with  $\omega_x = 0.20$ ,  $\omega_y = \omega_z = 0.01$  MeV/ $\hbar$ , corresponding to the upper panels of Fig. 8 (left panel), and with  $\omega_x = \omega_y = 0.01$ ,  $\omega_z = 0.20$  MeV/ $\hbar$ , corresponding to the lower panels of Fig. 9 (right panel). The energy of the experimental TSD1 is also included in both panels.

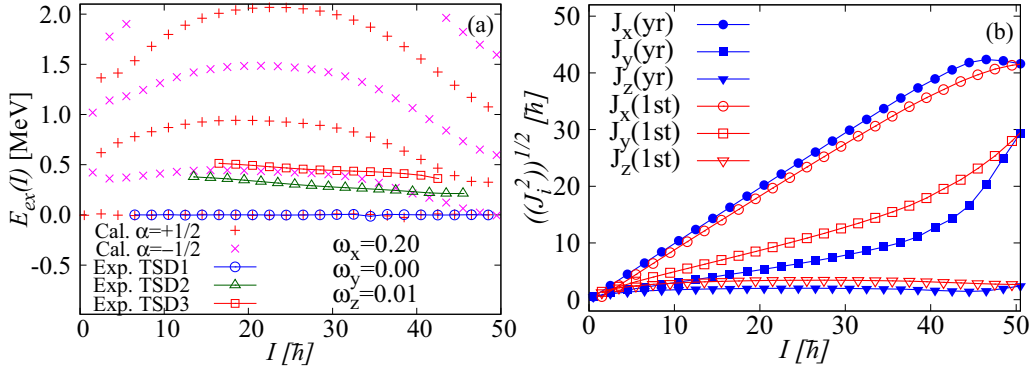


FIG. 11. The calculated excitation energy (left panel) and the expectation values (right panel) of the angular-momentum vector for the cranked mean-field with  $\omega_x = 0.20$ ,  $\omega_y = 0.0$ ,  $\omega_z = 0.01$  MeV/ $\hbar$  in  $^{163}\text{Lu}$ . The experimental excitation energies of TSD1, TSD2, and TSD3 are also included in the left panel.

$I \rightarrow I - 1$  are also larger than those with  $I \rightarrow I + 1$ , but the calculated values of the  $B(M1)$  ratio are about one order of magnitude larger than the measured values: The measured values of the  $B(M1 : I \rightarrow I - 1)$  are of the same order of magnitude as the calculated values for  $I \rightarrow I + 1$  transitions. These results are very similar to those obtained in the previous calculation [25], where another microscopic approach, the QRPA formalism, is employed. It should be emphasized that in both the QRPA and the present projection method the obtained results for  $B(E2)$  strongly support the validity of the basic picture of the simple triaxial-rotor model (see also Ref. [14] for the similar conclusion). Recently, it was suggested [36] that the inclusion of the isovector-type schematic interaction composed of the orbital angular momentum resolves the difficulty of an order of magnitude overestimation of the out-of-band  $B(M1)$  values, but we were not able to confirm it. Further study of this point is needed.

The almost constant in-band  $B(E2)$  values and the  $1/I$ -decreasing trend of the out-of-band  $B(E2)$  values are the result of the fixed triaxial deformation and the fixed rotational axis (see, e.g., Refs. [1,26]). The dominance of  $I \rightarrow I - 1$  transitions for the out-of-band  $B(E2)$  and  $B(M1)$  values is characteristic for the positive- $\gamma$  rotation, namely, the rotation about the short axis ( $x$  axis with  $0 < \gamma < 60^\circ$ ). This feature

is realized for the transverse wobbling. If the nucleus rotates around the largest-inertia axis (medium axis) of the core ( $y$  axis with  $0 < \gamma < 60^\circ$ ), the  $I \rightarrow I + 1$  out-of-band transitions dominate in the rotor model [1,26]: This feature is realized for simple wobbling of the core (even-even nucleus) [14] and also for the longitudinal wobbling. Since the rotation axis is quite often chosen to be the  $x$  axis for the study of the high-spin states, such a rotation scheme around the largest inertia axis corresponds to the triaxial deformation with  $-60^\circ < \gamma < 0$ , i.e., the negative- $\gamma$  rotation. Therefore, which out-of-band  $B(E2)$  transition is stronger, that with  $I \rightarrow I + 1$  or with  $I \rightarrow I - 1$ , is crucial to distinguish the positive- $\gamma$  or negative- $\gamma$  rotation, which was first emphasized in Ref. [44]. In the case of the odd- $A$  nucleus with a highly alignable quasiparticle, these positive- $\gamma$  and negative- $\gamma$  rotations just correspond to the difference between the transverse and longitudinal wobbling, respectively, and the observed data for  $^{163}\text{Lu}$  clearly indicate transverse wobbling [20].

In this way, the axis of rotation is also important for the electromagnetic properties of the nuclear wobbling motion. Although it does not correspond to the observed case in  $^{163}\text{Lu}$ , we show in Fig. 14 the in-band  $B(E2)$  values and the out-of-band to in-band  $B(E2)$  ratios for the case of the infinitesimally cranked mean field with  $\omega_x = \omega_y = \omega_z = 0.01$  MeV/ $\hbar$ , for

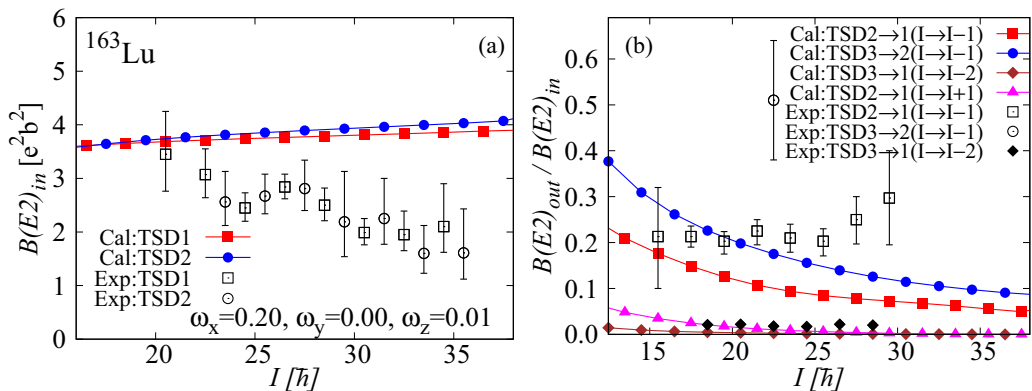


FIG. 12. The  $I \rightarrow I - 2$  in-band  $E2$  transition probabilities (left panel) and the  $I \rightarrow I \pm 1$  out-of-band to in-band  $B(E2)$  ratios (right panel) are compared with the experimental data in  $^{163}\text{Lu}$ . The cranked mean field with the frequencies  $\omega_x = 0.20$ ,  $\omega_y = 0.0$ ,  $\omega_z = 0.01$  MeV/ $\hbar$  are used, corresponding to Fig. 11. The experimental data are taken from Refs. [37,38,42].

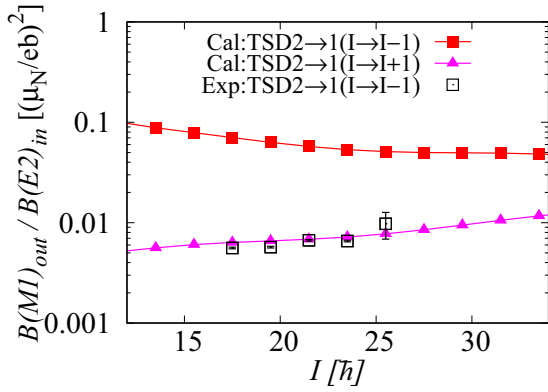


FIG. 13. The  $I \rightarrow I \pm 1$  out-of-band  $B(M1)$  to in-band  $B(E2)$  ratios are compared with the experimental data in  $^{163}\text{Lu}$ . The cranked mean field with the frequencies  $\omega_x = 0.20$ ,  $\omega_y = 0.0$ ,  $\omega_z = 0.01$  MeV/ $\hbar$  are used, corresponding to Fig. 11. The experimental data are taken from [42].

which the excitation spectrum and the expectation values of the angular-momentum vector are shown in the lower panels of Fig. 7. In this case, the in-band  $B(E2)$  values in the left panel of Fig. 14 increase as a function of spin even if the deformation is kept constant. This is because the main component of the angular-momentum vector in the intrinsic frame changes from that of the  $x$  axis to the  $y$  axis, as shown in the lower right panel of Fig. 7. The in-band  $B(E2)$  values are proportional to  $|(y^2 - z^2)|^2$  when rotating around the  $x$  axis, while they are proportional to  $|(z^2 - x^2)|^2$  when rotating around the  $y$  axis. The latter is larger for the present triaxial deformation with  $\gamma(\text{WS}) = 18^\circ$ . Therefore, the gradual change of the rotation axis from the  $x$  axis to the  $y$  axis increases the in-band  $B(E2)$  value, as displayed in the left panel of Fig. 14. This effect is visible as very tiny effect in Fig. 12. The in-band  $B(E2)$  values only slightly increase as a function of spin due to the gradual increase of the component of the angular momentum along the  $y$  axis in the right panel of Fig. 11. Although the absolute value of the out-of-band  $B(E2)$  is too small in this case, the effect of changing the rotation axis is even more drastic for the out-of-band  $B(E2)$  as shown in the right panel of

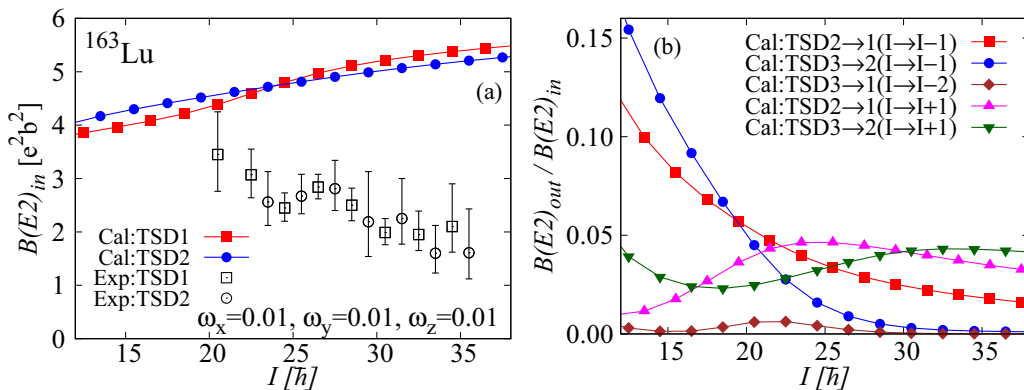


FIG. 14. The  $I \rightarrow I - 2$  in-band  $E2$  transition probabilities (left panel) and the  $I \rightarrow I \pm 1$  out-of-band to in-band  $B(E2)$  ratios (right panel) in  $^{163}\text{Lu}$ . The cranked mean field with the frequencies,  $\omega_x = \omega_y = \omega_z = 0.01$  MeV/ $\hbar$ , are used, corresponding to the lower panels of Fig. 7. Note that the scale for the  $B(E2)$  ratios is enlarged from that in Fig. 12.

Fig. 14. The dominance of the  $I \rightarrow I - 1$  or of the  $I \rightarrow I + 1$  transitions exchanges near the critical angular momentum of the vanishing one-phonon energy,  $I_c \approx 22$ , in the lower panel of Fig. 7. The  $I \rightarrow I + 1$  out-of-band  $B(E2)$  values of both the transitions from TSD2 to TSD1 and from TSD3 to TSD2 are much larger for  $I \gtrsim I_c$  in contrast to the opposite feature at low spins.

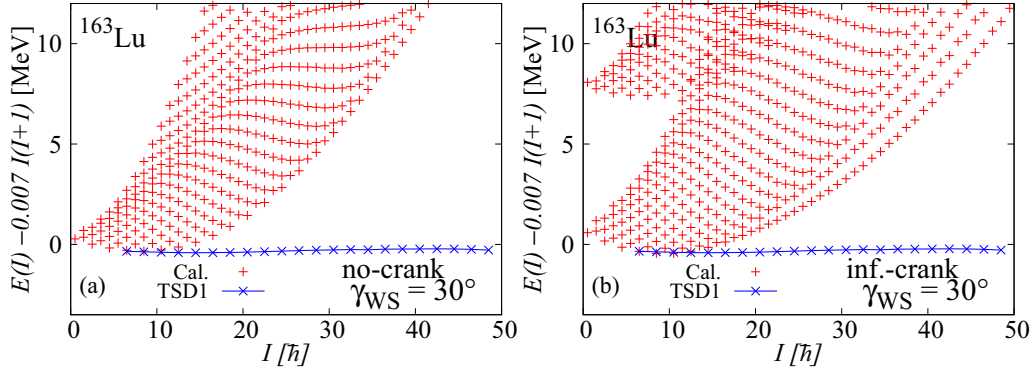
#### D. Results with larger $\gamma$ deformation

Until now, we have used the triaxial deformation in Eq. (15), which is the self-consistent value for the Nilsson or Woods-Saxon–Strutinsky method. The triaxiality parameter also affects the wobbling motion, especially the  $B(E2)$  values [1]. Therefore, we show here some results of the projection calculation with larger triaxial deformation for the mean field. We choose rather arbitrarily  $\gamma(\text{WS}) = 30^\circ$ , keeping the other deformation parameters  $\beta_2 = 0.42$  and  $\beta_4 = 0.02$ . It is noted again that  $\gamma(\text{WS}) = 30^\circ$  of the Woods-Saxon potential corresponds to smaller triaxial deformation of the density distribution; for  $\beta_2 \sim 0.42$ ,

$$\gamma(\text{WS}) \sim 30^\circ \Leftrightarrow \gamma(\text{den}) \sim 21 - 22^\circ. \quad (20)$$

It should be mentioned that the positive-parity proton orbit at the Fermi surface is not the one originating from the  $i_{13/2}$  state for  $[\beta_2, \beta_4, \gamma(\text{WS})] = (0.42, 0.02, 30^\circ)$ , which is crossed at  $\gamma(\text{WS}) \approx 25^\circ$  by a orbit which is mainly of  $N_{\text{osc}} = 4$  (see Fig. 1 of Ref. [25]). We choose to occupy the second excited quasiparticle near the Fermi surface originating from the  $i_{13/2}$  particle for an odd proton, which is necessary to realize the TSD states.

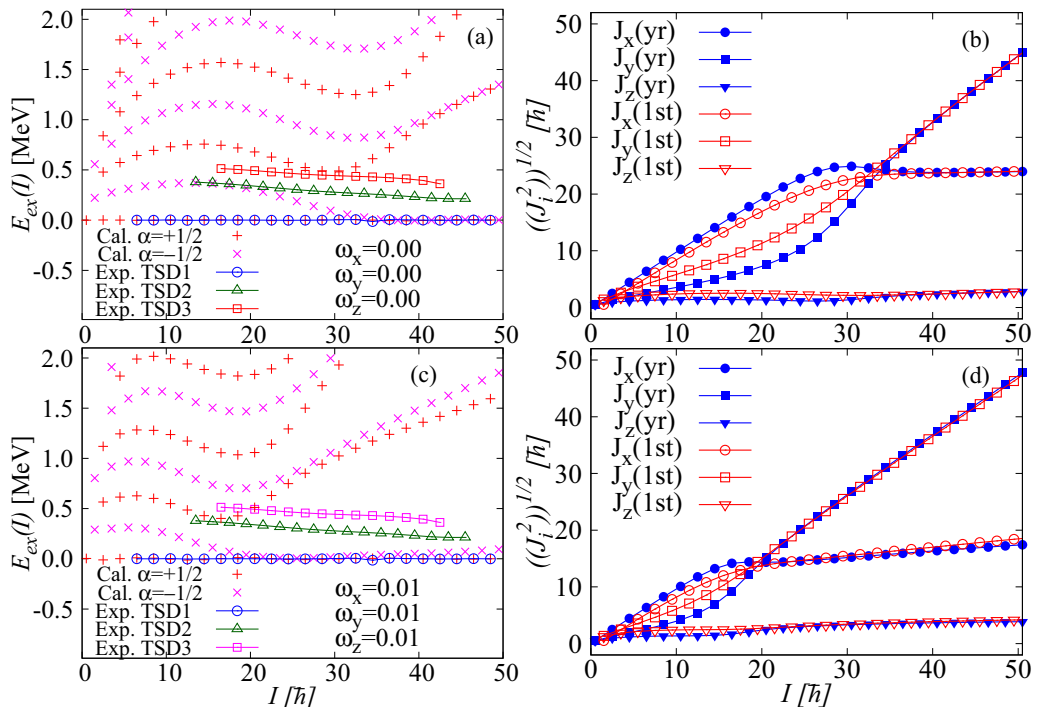
In Fig. 15, we show the calculated spectrum with the noncranked mean field (left panel) and with the infinitesimally cranked mean field with  $\omega_x = \omega_y = \omega_z = 0.01$  MeV/ $\hbar$  (right panel), just like in Fig. 6. As in the case of  $\gamma(\text{WS}) = 18^\circ$ , the multiple band structure characteristic for the wobbling motion appears. Compared with Fig. 6, the moments of inertia for the rotational bands are slightly smaller in Fig. 15 than in Fig. 6. This can be naturally understood. As already studied in the previous section, the main rotation axis is the short ( $x$ ) axis due to the presence of the aligned  $\pi i_{13/2}$  particle, and the core


 FIG. 15. Same as Fig. 6 but the result of projection from the mean field with larger triaxial deformation  $\gamma(\text{WS}) = 30^\circ$ .

moment of inertia around this axis decreases as a function of  $\gamma$ ; see Fig. 1. However, the value of the cranking inertia of the  $x$  axis does not change so much at  $\gamma(\text{WS}) = 30^\circ$  compared with that at  $\gamma(\text{WS}) = 18^\circ$  because of the bumplike behavior in Fig. 1. Therefore, the moments of inertia of the wobbling bands are only slightly reduced in Fig. 15 in comparison with those in Fig. 6.

The excitation spectrum and the expectation values of the angular-momentum components in the intrinsic frame are displayed in the upper and lower panels of Fig. 16 for the cases of the noncranked and infinitesimally cranked mean fields, respectively. By comparing Figs. 7 and 16, it can be seen that the excitation energy of the wobbling phonon is smaller for the mean field with larger triaxiality,  $\gamma(\text{WS}) = 30^\circ$ , i.e., the wobbling-phonon excitation energy decreases when the triaxiality increases. Because of this, the critical angular momentum of the vanishing one-phonon excitation energy

is shifted to lower spins in Fig. 16. It is worth mentioning that in the case of larger triaxial deformation of Eq. (20), the excitation spectrum after the critical frequency is different from the one in the case of smaller triaxial deformation of Eq. (15). The signature partner bands with  $\alpha = \pm \frac{1}{2}$  are almost degenerate after the critical spin in this case, i.e., there is one  $\Delta I = 1$  band instead of two  $\Delta I = 2$  bands, for  $I \gtrsim 32$  in the upper panels of Fig. 16 and for  $I \gtrsim 20$  in the lower panels of Fig. 16, while the signature splittings are significant in Fig. 7, even though the behavior of the expectation values of angular-momentum vectors are rather similar in Figs. 16 and 7. The ‘signature quantum number’ is severely broken in the case of larger triaxial deformation in Fig. 16. We think that the reason is the following: In the present case, the component of angular momentum along the long axis ( $z$  axis) is always small, so that the rotational axis lies in the  $xy$  plane. If both the  $x$  and  $y$  components are sizable, the symmetry with respect to the  $180^\circ$


 FIG. 16. Same as Fig. 7 but the result of projection from the mean field with larger triaxial deformation  $\gamma(\text{WS}) = 30^\circ$ .

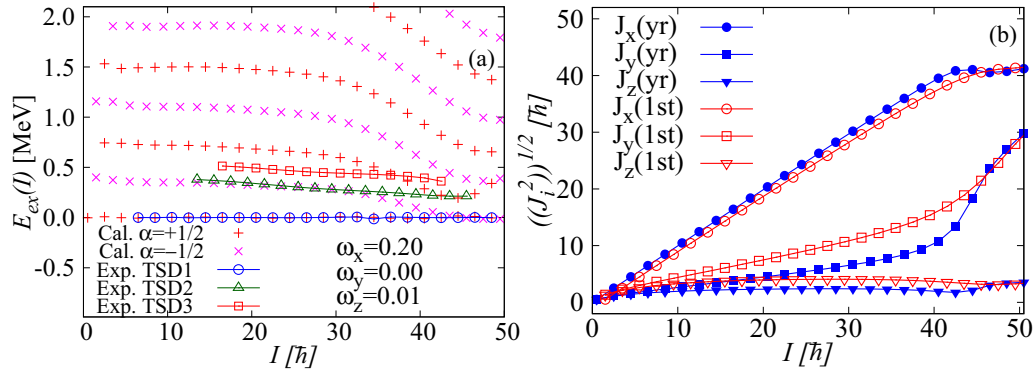


FIG. 17. Same as Fig. 11 but the result of projection from the mean field with larger triaxial deformation  $\gamma(\text{WS}) = 30^\circ$ .

rotation around the rotation axis is broken. However, if the mean field is axially symmetric about the  $z$  axis, the signature symmetry is still present. In the case of the smaller triaxial deformation in Eq. (15) [ $\gamma(\text{den}) \approx 11 - 12^\circ$ ], the signature symmetry is not so strongly broken and sizable signature splitting appears for the wobbling bands based on the highly alignable  $\pi i_{13/2}$  particle. In contrast, the triaxial deformation in Eq. (20) [ $\gamma(\text{den}) \approx 21 - 22^\circ$ ] is large enough to strongly break the signature symmetry. The signature splitting is getting sizable at highest spins displayed in the lower panels of Fig. 16, because the  $x$  component is getting smaller compared to the  $y$  component and the nucleus rotates mainly around the principal  $y$  axis, which makes the signature an approximately good quantum number again. Thus, these are interesting examples of the interplay of the dynamical motion of the angular-momentum vector and the triaxial deformed mean field in the intrinsic frame.

It is well known that the effect of triaxial deformation is more important for the  $E2$  transition probabilities [1]. As in the previous case of smaller triaxial deformation, we present, for the case of larger triaxiality  $\gamma(\text{WS}) = 30^\circ$ , the result of projection from the cranked mean field with  $\omega_x = 0.20$ ,  $\omega_y = 0.0$ ,  $\omega_z = 0.01$  MeV/ $\hbar$ , in which the value of the critical angular momentum is relatively large and still the one-phonon excitation energy is relatively low. We first show in Fig. 17 the excitation spectrum and the expectation values of the angular-momentum vector in the intrinsic frame, just like in Fig. 11, where the triaxiality is smaller,  $\gamma(\text{WS}) = 18^\circ$ . As in the case of the noncranked or of the infinitesimally cranked mean field, the excitation energies are smaller and the agreement of the TSD1 excitation energy is better, although the calculated TSD2 excitation energies are still higher than the experimental data. The calculated in-band  $B(E2)$  values and the out-of-band to in-band  $B(E2)$  ratios are compared with the experimental data in Fig. 18. Comparing in-band  $B(E2)$  values for the cases with  $\gamma(\text{WS}) = 18^\circ$  and  $30^\circ$  in the left panels of Figs. 12 and 18, the latter is considerably smaller. This can be understood by the rotor model [1]. As the rotation axis is mainly the  $x$  axis in both cases (see the right panels of Figs. 11 and 17), the  $B(E2)$  values are proportional to  $|(y^2 - z^2)|^2 \propto \cos^2(\gamma + 30^\circ)$ , which is a decreasing function of  $\gamma$  for  $0 < \gamma < 60^\circ$ . On the other hand, the out-of-band to in-band  $B(E2)$  ratios are considerably larger for larger  $\gamma$  deformation, which can be also understood by the

rotor model [1]. The large average value of  $B(E2)_{\text{out}}/B(E2)_{\text{in}}$  ratios for the TSD2 to TSD1 transitions, which is considered to be crucial to identify the wobbling motion, is better described by the calculation with the larger  $\gamma$  value in Eq. (20). The calculated  $B(M1)_{\text{out}}/B(E2)_{\text{in}}$  ratios are about factor two larger for the  $I \rightarrow I - 1$  transitions than for  $\gamma(\text{WS}) = 18^\circ$  (not shown), while those for the  $I \rightarrow I + 1$  transitions are similar; i.e., the overestimation of the  $B(M1)$  values is a little bit more serious.

The experimental in-band  $B(E2)$  values decrease as a function of spin, and  $B(E2)_{\text{out}}/B(E2)_{\text{in}}$  ratios are almost constant or even increase at the highest spins. It is very difficult to reproduce these trends in the calculation as long as constant deformation is assumed. It is discussed [25] that a considerable increase of the  $\gamma$  deformation as a function of spin can explain these features of the in-band and out-of-band  $B(E2)$  values, although the self-consistent mean-field calculations suggest that the deformation does not change so much. In order to perform the angular-momentum-projection calculation for such mean field changing with spin, one has to prepare several mean fields with different triaxiality  $\gamma$  and employ the configuration-mixing calculation like in Ref. [14], where no cranking is performed. Such calculations combined with the finite cranking frequencies are interesting but out of scope in the present investigation.

### E. Example for the case of the odd proton in a nonintruder orbit

For the sake of completeness we briefly discuss the spectrum obtained by projection from the mean-field state, where the odd proton in  $^{163}\text{Lu}$  does not occupy the high- $j$  intruder orbit  $i_{13/2}$ . As mentioned in the previous subsection, the lowest proton orbit near the Fermi surface at  $\gamma(\text{WS}) = 30^\circ$  originates mainly from  $N_{\text{osc}} = 4$  (see Fig. 1 of Ref. [25]). This relatively low- $j$  orbit is now occupied by the odd proton quasiparticle to generate the mean-field state, from which the projection calculation is performed.

Figure 19 displays the calculated spectrum with the noncranked mean-field (left panel) and with the infinitesimally cranked mean field with  $\omega_x = \omega_y = \omega_z = 0.01$  MeV/ $\hbar$  (right panel) just like in Figs. 6 and 15. The multiple-band structure emerges in both cases as in the previous cases. However, apparently the slopes of the wobbling bands are steeper than



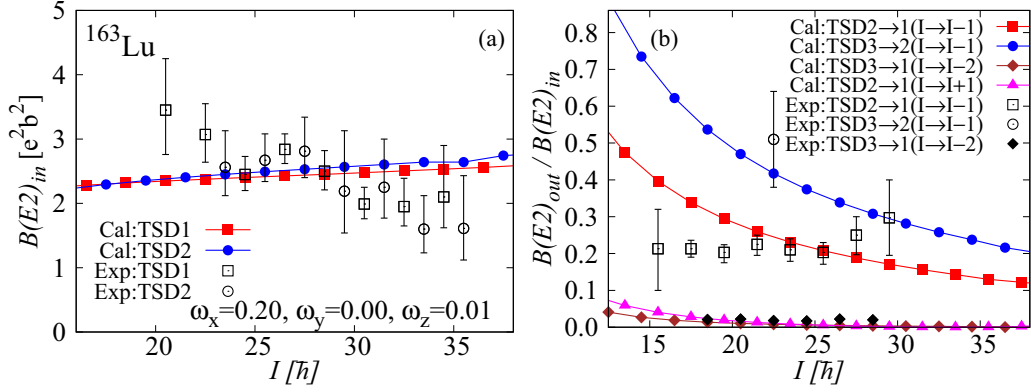


FIG. 18. Same as Fig. 12 but the result of projection from the mean field with larger triaxial deformation  $\gamma(\text{WS}) = 30^\circ$ .

those in Fig. 15; namely, their calculated moments of inertia are even smaller than the case with the high- $j$  orbit being occupied. The lowest energy state has  $I^\pi = 1/2^+$  for the case of no cranking and  $I^\pi = 3/2^+$  for the case of infinitesimal cranking.

The excitation energies and the expectation values of the angular-momentum components in the intrinsic frame are displayed in the upper and lower panels of Fig. 20 for the cases of the noncranked and of the infinitesimally cranked mean field, respectively. The dominant component of the angular momentum is always along the largest inertia axis ( $y$  axis) in both cases, and, consequently, the excitation energies increase monotonically as functions of spin, just like for the even-even core nucleus. The odd proton aligns its angular-momentum vector mainly along the  $y$  axis, although the alignment is rather small, and this case roughly corresponds to the longitudinal wobbling. In this way, the basic picture of the transverse wobbling and of the longitudinal wobbling, proposed in Ref. [20] and discussed in Sec. III A, is justified by our fully microscopic calculations in the framework of the angular-momentum-projection method. It is interesting to mention that the signatures of the yrast and excited bands are  $\alpha = +1/2, -1/2, -1/2, +1/2, +1/2, \dots$  in the result with the noncranked mean field in the upper left panel of Fig. 20, which is different from the simple alternating pattern in the case of occupying the high- $j$  intruder orbit. This is because the nonintruder orbit of the odd proton is a strongly mixed

state of the spherical shell-model orbits,  $s_{1/2}$ ,  $d_{3/2}$ ,  $d_{5/2}$ , and  $g_{7/2}$ , and its angular momentum  $j$  is not definite. Consequently, the coupling scheme between the angular momenta of the odd proton and the even-even core is not so simple as in the case of the high- $j$  intruder orbit. Moreover, the excitation energy of the second excited band is smaller than twice the excitation energy of the first excited band. In contrast, the alternating pattern of the signatures is recovered with the infinitesimal cranking in the lower left panel of Fig. 20, and the second wobbling energy is considerably larger than twice the first wobbling energy. At present, we do not see a clear reason why this kind of qualitative difference appears as a result of the infinitesimal cranking.

### F. Result with Gogny D1S interaction

It is known that the density-dependent term in the Gogny or Skyrme interactions causes fundamental problems for beyond mean-field calculations including the angular-momentum projection (see, e.g., Refs. [45,46] and references therein). The problem seems to be more serious for odd and odd-odd nuclei than for even-even nuclei. Although infinitesimal cranking around all three principal axes has been applied in the even-even nucleus  $^{164}\text{Er}$  in Ref. [14], we found for  $^{163}\text{Lu}$  that infinitesimal cranking with respect to more than one axis suffers from these problems. We were able to obtain reasonable result of the projection calculation for the mean field with only one-dimensional cranking. Therefore, we only show the

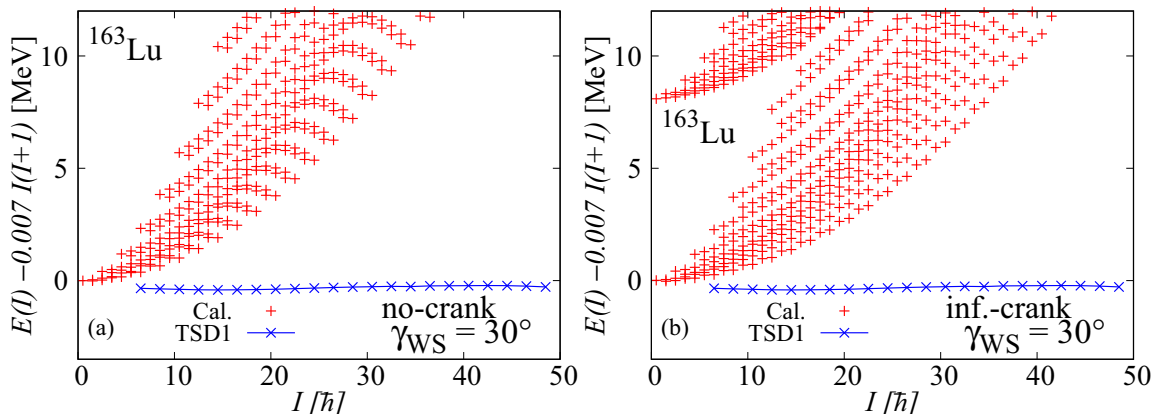
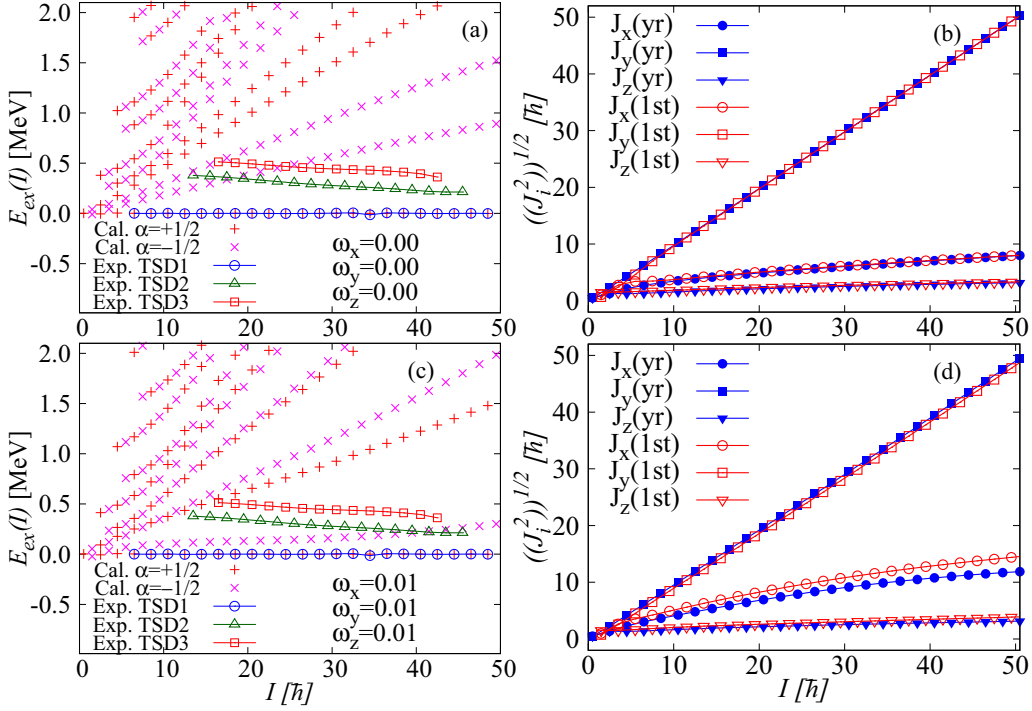


FIG. 19. Same as Fig. 15 but the odd-proton particle occupies low- $j$  orbit in this calculation.

FIG. 20. Same as Fig. 16 but the odd-proton particle occupies low- $j$  orbit in this calculation.

result of such a case. All the calculations have been done by expanding the HFB states within the isotropic harmonic oscillator basis as for the calculation of the Woods-Saxon mean field. We have used the same model space composed of the basis states with the maximum oscillator shells up to  $N_{\text{osc}}^{\text{max}} = 12$ .

In this Gogny-HFB approach, the mean-field potential is generated by the self-consistent HFB procedure. Since the  $\pi i_{13/2}$  particle favors aligning its angular-momentum along the short ( $x$ ) axis, we have performed the Gogny HFB calculation by blocking the lowest positive-parity quasiproton with  $x$  axis cranking. With finite rotational frequencies, we have found essentially the same TSD mean-field parameters as obtained by the Nilsson-Strutinsky calculation [e.g., in Ref. [43]; note the relation of the triaxiality parameter in Eq. (15)]. We were not able to obtain a convergent solution near zero rotational frequency. The average pairing gaps in Eq. (11)

and deformation parameters in Eq. (10) of the HFB mean field are tabulated in Table I as functions of the rotational frequency  $\omega_x$ , where the expectation value of the angular momentum  $\langle J_x \rangle$  is also included. Clearly there exists aligned angular momentum along the  $x$  axis of the odd  $i_{13/2}$  proton. Note that for one-dimensional cranking around the  $x$  axis, all nonzero deformation parameters are real. Here the parameters  $(\beta_2, \gamma)$  are determined, as usual, by  $\beta_2(\text{den}) \equiv [\alpha_{20}(\text{den})^2 + 2\alpha_{22}(\text{den})^2]^{1/2}$  and  $\gamma(\text{den}) \equiv \tan^{-1}[-\sqrt{2}\alpha_{22}(\text{den})/\alpha_{20}(\text{den})]$ , which is exactly the same as in Eq. (14). The average pairing gaps at the lowest frequency,  $\omega_x = 0.05$  MeV/ $\hbar$ , for both neutrons and protons are smaller than the even-odd mass differences of the ground states in the neighboring even-even nuclei. The proton gap is especially small because of the blocking effect. The proton (neutron) pairing correlations vanish for  $\omega_x \gtrsim 0.25$  ( $\omega_x \gtrsim 0.40$ ) MeV/ $\hbar$  as it is shown in Table I. The obtained triaxiality parameter  $\gamma(\text{den})$  just corresponds to the

TABLE I. The expectation value  $\langle J_x \rangle$ , the neutron and proton average pairing gaps in Eq. (11), and nuclear radius and various nonzero deformation parameters in Eq. (10) with  $\lambda \leq 4$  as functions of the rotational frequency with respect to the  $x$  axis,  $\omega_x$ , of mean field obtained by the cranked Gogny-HFB calculation for the TSD yrast states of  $^{163}\text{Lu}$ .

$\omega_x$ [MeV]	$\langle J_x \rangle$ [ $\hbar$ ]	$\bar{\Delta}_n$ [MeV]	$\bar{\Delta}_p$ [MeV]	$\bar{R}$ [fm]	$\beta_2$ (den)	$\gamma$ (den)	$\alpha_{40}$ (den)	$\alpha_{42}$ (den)	$\alpha_{44}$ (den)
0.050	8.1	0.776	0.496	6.880	0.443	10.7°	0.162	-0.0394	-0.00386
0.100	11.1	0.753	0.470	6.880	0.443	10.9°	0.163	-0.0406	-0.00373
0.150	14.1	0.722	0.416	6.880	0.443	11.0°	0.162	-0.0416	-0.00359
0.200	17.3	0.677	0.322	6.880	0.443	11.2°	0.160	-0.0429	-0.00342
0.250	20.8	0.610	0.0867	6.878	0.442	11.4°	0.157	-0.0449	-0.00320
0.300	24.4	0.515	0.000	6.877	0.440	11.7°	0.156	-0.0470	-0.00305
0.350	28.0	0.373	0.000	6.874	0.438	12.0°	0.155	-0.0494	-0.00310
0.400	31.7	0.0536	0.000	6.870	0.434	12.3°	0.154	-0.0520	-0.00366

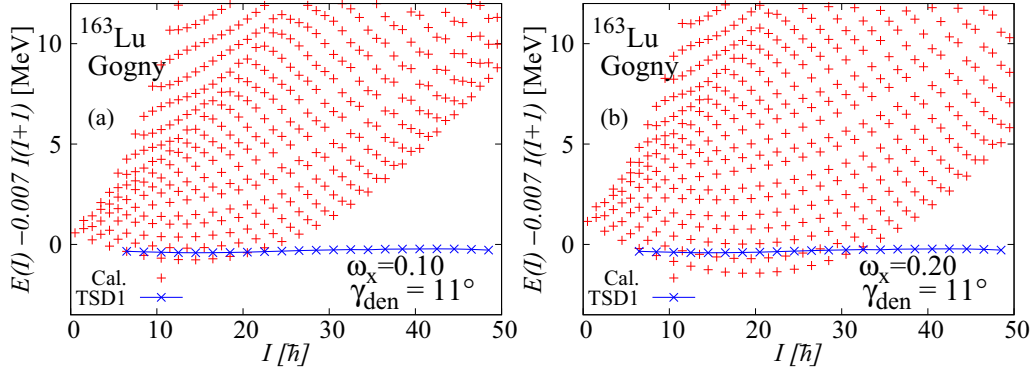


FIG. 21. Wobbling spectrum for  $^{163}\text{Lu}$  calculated by the angular-momentum-projection method with the Gogny D1S effective interaction. The cranked mean field with  $\omega_x = 0.10$  ( $\omega_x = 0.20$ ),  $\omega_y = \omega_z = 0.0$  MeV/ $\hbar$  is employed in the left (right) panel. The energy of the experimental TSD1 [37] is also included in each panel.

value in Eq. (15), and it is almost constant or only slightly increases as the frequency  $\omega_x$  increases, which is consistent with the result of Ref. [36] considering the different definition of the triaxiality parameter as it is mentioned in Eqs. (15) and (20); see Ref. [34] for the relation between  $(\beta_2(\text{WS}), \gamma(\text{WS}))$  [or  $(\beta_2(\text{Nils}), \gamma(\text{Nils}))$ ] and  $(\beta_2(\text{den}), \gamma(\text{den}))$ .

Figure 21 shows the calculated spectrum with using the Gogny-D1S interaction, where the mean field is cranked with the rotational frequencies  $\omega_x = 0.10$  ( $\omega_x = 0.20$ ),  $\omega_y = \omega_z = 0.0$  MeV/ $\hbar$  in the left (right) panel (see the mean-field parameters in Table I). The multiple-band structure, which is characteristic for the nuclear wobbling motion, emerges

also in this case. Compared with the result of the Woods-Saxon mean field and the schematic interaction in Fig. 6 or in Fig. 10, the slopes of the wobbling bands are less steep. Namely, the moments of inertia are larger in the result with the Gogny-D1S interaction;  $\mathcal{J}^{(1)} \approx 51\hbar^2/\text{MeV}$  at  $I \approx 20$  for the calculation with  $\omega_x = 0.10$  MeV/ $\hbar$  (the left panel), and  $\mathcal{J}^{(1)} \approx 65\hbar^2/\text{MeV}$  with  $\omega_x = 0.20$  MeV/ $\hbar$  (the right panel).

The excitation energy and the expectation values of the angular-momentum vector in the intrinsic frame are displayed in the upper and lower panels of Fig. 22, for the case of the cranking frequency  $\omega_x = 0.10$  and  $0.20$  MeV/ $\hbar$ , respectively. Clearly the phonon excitations can also be seen for the

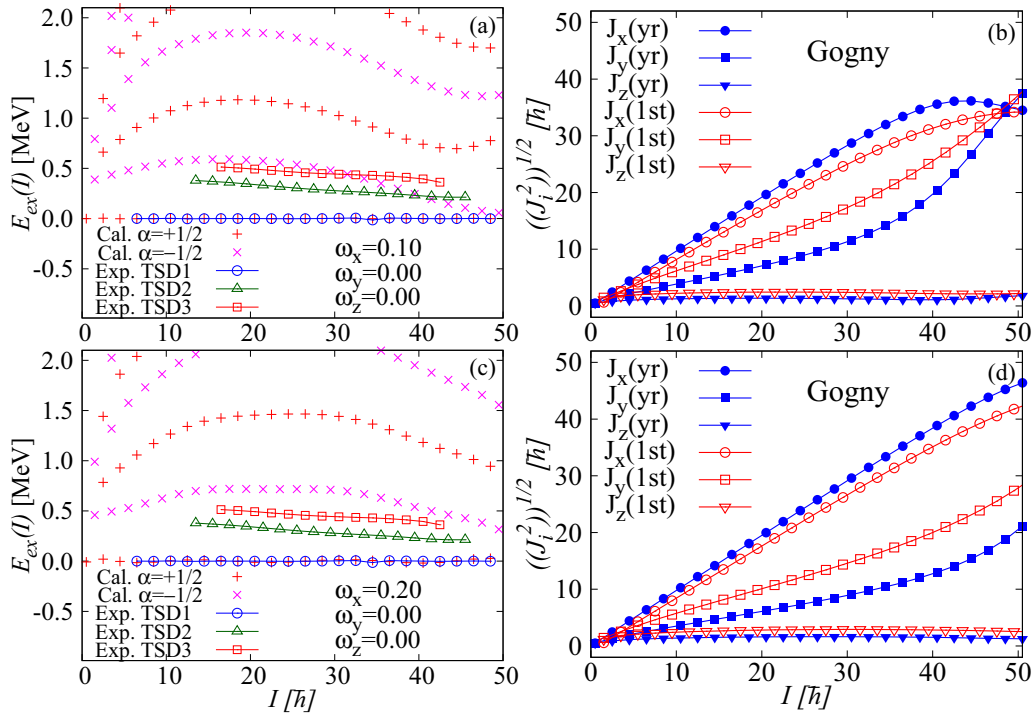


FIG. 22. The calculated excitation energy (left panels) and the expectation values of the angular-momentum vector (right panels) with using the Gogny-D1S interaction in  $^{163}\text{Lu}$ . The mean field is cranked with the frequencies,  $\omega_x = 0.10$ ,  $\omega_y = \omega_z = 0.0$  MeV/ $\hbar$  (upper panels) and  $\omega_x = 0.20$ ,  $\omega_y = \omega_z = 0.0$  MeV/ $\hbar$  (lower panels), The experimental excitation energies of TSD1, TSD2, and TSD3 [37] are also included in the left panels.

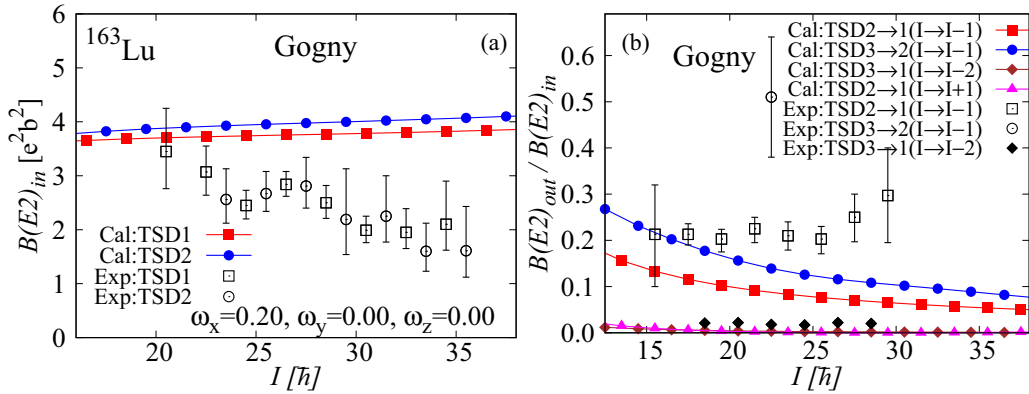


FIG. 23. The  $I \rightarrow I - 2$  in-band  $E2$  transition probabilities (left panel) and the  $I \rightarrow I \pm 1$  out-of-band to in-band  $B(E2)$  ratios (right panel), which are calculated with the Gogny-D1S interaction, are compared with the experimental data in  $^{163}\text{Lu}$ . The cranked mean field with the frequencies,  $\omega_x = 0.20$ ,  $\omega_y = \omega_z = 0.00$  MeV/ $\hbar$ , are used corresponding to the lower panels of Fig. 22.

calculation with using the Gogny-D1S interaction, where the excitation energy first increases and then decreases, showing the characteristic behavior of transverse wobbling. Apparently the resultant excitation spectrum is very similar to the one in the case of the Woods-Saxon mean field and the schematic interaction. The critical point of vanishing one-phonon excitation energy just corresponds to the point where the main component of the expectation values of the angular-momentum vector changes from the  $x$  axis to the  $y$  axis as shown in the right panels in Fig. 22. The excitation energy increases when the cranking frequency  $\omega_x$  is increased in the same way as in the case of the Woods-Saxon mean field.

We show the in-band  $B(E2)$  values and the out-of-band to in-band  $B(E2)$  and  $B(M1)$  ratios for the calculation using the Gogny-D1S interaction in Figs. 23 and 24, which are calculated for the mean field with  $\omega_x = 0.20$ ,  $\omega_y = \omega_z = 0.0$  MeV/ $\hbar$ , corresponding to the excitation spectrum in the lower panels of Fig. 22. The in-band  $B(E2)$  values and the  $B(E2)_{\text{out}}/B(E2)_{\text{in}}$  ratios are very similar to the ones of the Woods-Saxon mean field in Figs. 12. The  $B(M1)_{\text{out}}/B(E2)_{\text{in}}$  ratios are also similar,

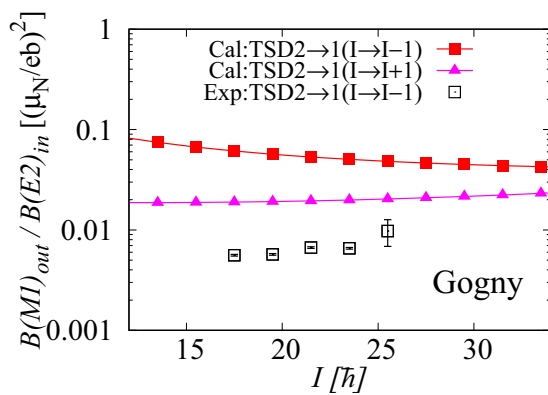


FIG. 24. The  $I \rightarrow I \pm 1$  out-of-band  $B(M1)$  to in-band  $B(E2)$  ratios calculated with the Gogny-D1S interaction, are compared with the experimental data in  $^{163}\text{Lu}$ . The cranked mean field with the frequencies  $\omega_x = 0.20$ ,  $\omega_y = \omega_z = 0.0$  MeV/ $\hbar$ , are used, corresponding to the lower panels of Fig. 22.

although the ratio with  $I \rightarrow I - 1$  transition are slightly smaller and that with  $I \rightarrow I + 1$  transition are larger than those in Fig. 13. All the characteristic features of the excitation energy spectrum and of the transition probabilities are the same as in the case of the Woods-Saxon mean field and the schematic interaction. If the same cranking frequencies are used in the Woods-Saxon mean field, i.e.,  $\omega_x = 0.20$ ,  $\omega_y = \omega_z = 0.0$  MeV/ $\hbar$ , the results of the Gogny-HFB and the Woods-Saxon mean field are much more similar: The only difference is that the absolute value of the moment of inertia for the wobbling band is larger in the calculation with the Gogny interaction. This result clearly tells us that the wobbling motion calculated by the microscopic angular-momentum-projection method does not essentially depend on the details of the used effective interaction. Therefore, we confirmed that the rotor-model picture of the wobbling motion is validated by our microscopic projection calculations.

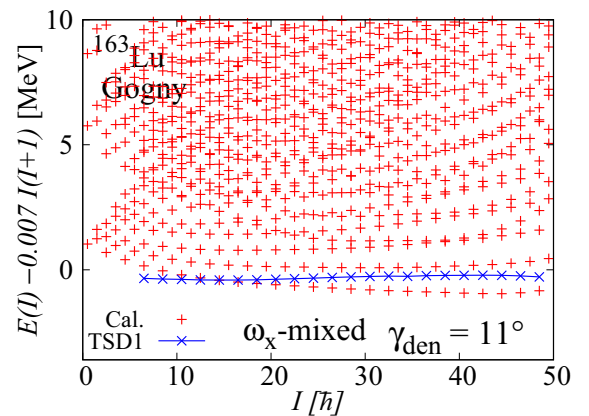


FIG. 25. Wobbling spectrum for  $^{163}\text{Lu}$  calculated by the angular-momentum-projection method with multicranked configuration mixing employing the Gogny-D1S effective interaction. The four cranked HFB states with  $\omega_x = 0.10, 0.25, 0.40, 0.55$  MeV/ $\hbar$  are configuration mixed. The energy of the experimental TSD1 [37] is also included.

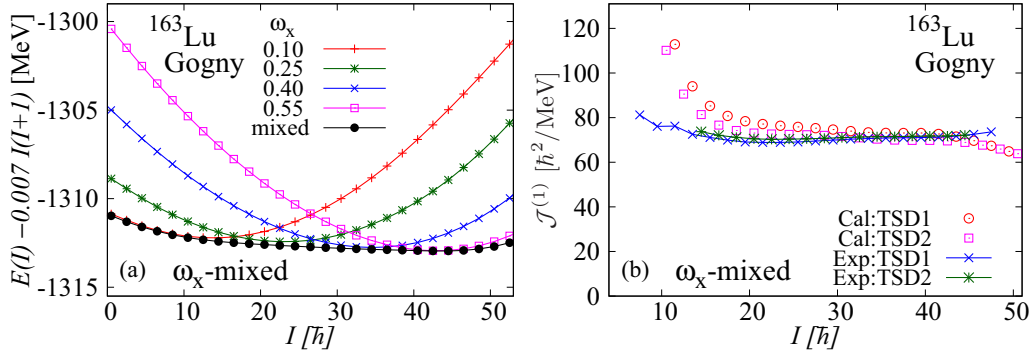


FIG. 26. Left panel: Absolute energy of the yrast band obtained by the multicranked configuration mixing in comparison with those calculated with a single HFB state with  $\omega_x = 0.10, 0.25, 0.40, 0.55$  MeV/ $\hbar$ . Right panel: Moments of inertia defined in Eq. (18) for the lowest two TSD bands calculated by the angular-momentum-projection method with multicranked configuration mixing corresponding to Fig. 25. The experimental data are also included for comparison.

### G. Multicranked configuration mixing with Gogny-D1S interaction

Recently, we have proposed the method of projected multicranked configuration mixing for a reliable description of the rotational band in Ref. [15], and it has been successfully applied to nuclei in the rare-earth-metal region employing the Gogny-D1S interaction [16]. One of the problems in the present investigation up to here is that the calculated moment of inertia of the TSD bands in  $^{163}\text{Lu}$  is considerably smaller than the measured one; see, e.g., Fig. 21. This is mainly because only one mean-field state is employed. In fact, the calculated inertia with a single mean-field state decreases as spin increases, for example,  $\mathcal{J}^{(1)} \approx 51$  (64)  $\hbar^2/\text{MeV}$  at  $I \approx 20$  while  $\mathcal{J}^{(1)} \approx 42$  (44)  $\hbar^2/\text{MeV}$  at  $I \approx 45$  if the cranking frequency  $\omega_x = 0.10$  (0.20) MeV/ $\hbar$  is used. The moment of inertia increases when the cranking frequency  $\omega_x$  is increased. Therefore, we have performed the multicranked configuration-mixing calculation including four cranked HFB states with cranking frequencies,  $\omega_x = 0.10, 0.25, 0.40, 0.55$  MeV/ $\hbar$ , in Eq. (13) with  $N_{\text{mf}} = 4$ .

The resultant spectrum is displayed in Fig. 25. Clearly, the lowest band nicely corresponds to the measured TSD1 band and the result is much better than those in Fig. 21. The level density of higher excited bands is considerably increased. Even

with a single mean-field wobbling bands appear at higher excitation energy if the cranking procedure is applied, as is shown in the previous sections (see, e.g., Fig. 6). If the four mean fields with different cranking frequencies are mixed, various higher quasiparticle configurations are effectively included and more excited multiple-wobbling bands are expected to come about. This is the reason of increasing level density. In order to see the effect of configuration mixing, we show the calculated yrast band before and after the mixing in the left panel of Fig. 26. It is clearly seen that the main configuration of the mixed band smoothly changes as a function of spin. The calculated moments of inertia  $\mathcal{J}^{(1)}$  are compared with the experimental data for the lowest two TSD bands in the right panel of Fig. 26. Rather good agreement is achieved, although the calculated moment of inertia is slightly overestimated in the low-spin region. Thus, the property of the rotational bands are better described by the present multicranked configuration mixing.

However, the spin dependence of the wobbling excitation energies shown in Fig. 27 are changed to increase monotonically compared with those in Fig. 22, and looks more like that of the original wobbling bands without the alignment or of the longitudinal wobbling, which are quite different from the experimental data. This change can be understood; it was already shown that if the higher cranking frequency  $\omega_x$  is

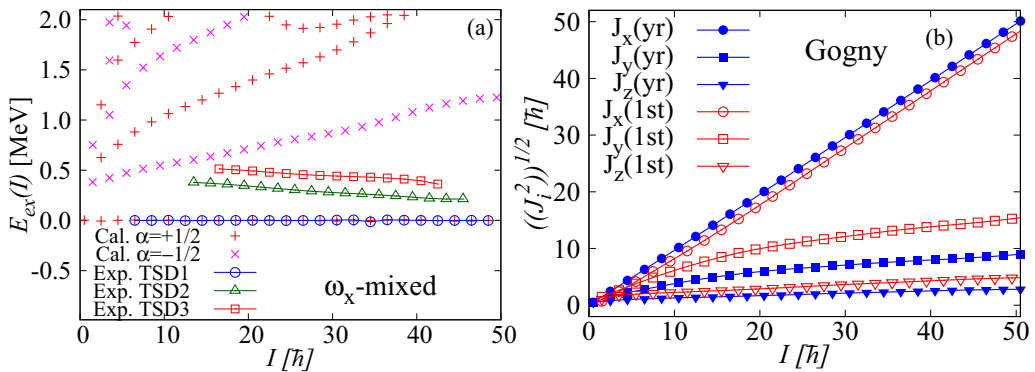


FIG. 27. The excitation energy (left) and the expectation values of the angular-momentum vector (right) in  $^{163}\text{Lu}$  calculated by the multicranked configuration mixing corresponding to Fig. 25. The experimental excitation energies of TSD1, TSD2, and TSD3 [37] are also included in the left panel.

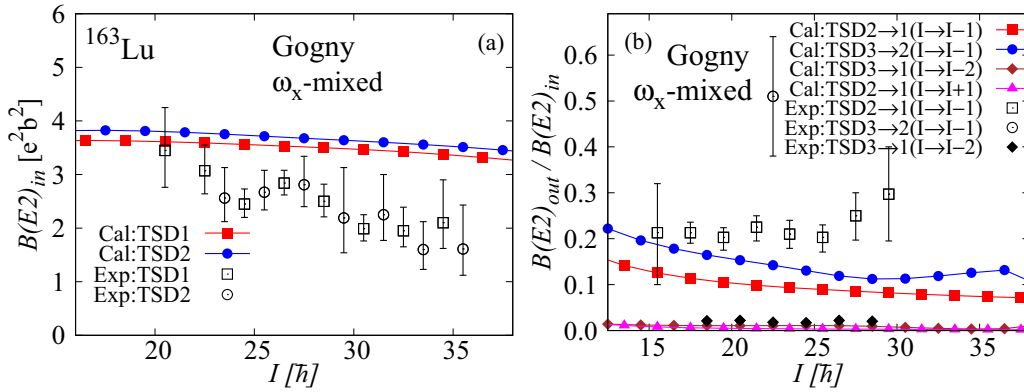


FIG. 28. The  $I \rightarrow I - 2$  in-band  $E2$  transition probabilities (left panel) and the  $I \rightarrow I \pm 1$  out-of-band to in-band  $B(E2)$  ratio (right panel), which are calculated by the multiranked configuration mixing with the Gogny-D1S interaction in  $^{163}\text{Lu}$ , corresponding to Fig. 25.

employed, the resultant wobbling excitation energy increases. Because the main component of the mixed band at higher spin states is composed of the projected states from the HFB state with higher cranking frequency, it is natural that the wobbling excitation energy increases when the spin increases. In fact, the main component of the angular-momentum vector is always along the  $x$  axis as is shown in the right panel of Fig. 27, and the direction of the vector never changes. Namely,  $((J_x^2))^{1/2} - ((J_y^2))^{1/2}$  increases monotonically and never decreases in the calculated spin range: This is the same behavior as in the case of the original wobbling or of the longitudinal wobbling, although the main component is along the short ( $x$ ) axis in Fig. 27 in contrast to the case, e.g., of Fig. 20, where the main component is along the medium ( $y$ ) axis.

The in-band  $B(E2)$  values and the out-of-band versus in-band  $B(E2)$  ratios calculated with the multiranked configuration mixing are depicted in Fig. 28. The out-of-band  $B(M1)$  ratio is slightly smaller at higher spins but still about one order of magnitude larger (not shown). Compared with the result obtained by the projection from a single HFB state (e.g., Fig. 23), the in-band  $B(E2)$  values very gradually decrease with spin because the  $\beta_2$  decreases and  $\gamma$  increases slightly as functions of the cranking frequency (see Table I). This trend continues at higher frequency,  $\omega_x \geq 0.40$  MeV/ $\hbar$ , e.g.,  $\beta_2(\text{den}) = 0.423$  and  $\gamma(\text{den}) = 13.1^\circ$ , and  $\langle J_x \rangle = 41.2 \hbar$  at  $\omega_x = 0.55$  MeV/ $\hbar$ . As for the  $B(E2)_{out}/B(E2)_{in}$  ratios, the results are not very different from those obtained by the projection from a single HFB state (e.g., in Fig. 23). The spin dependence is slightly changed; for example, the  $B(E2)_{out}/B(E2)_{in}$  ratios are a little bit larger at higher spins,  $I \gtrsim 25$ . In any case, as it is already discussed, the calculated self-consistent triaxial deformation is too small to account for the experimentally measured  $B(E2)_{out}/B(E2)_{in}$  ratios at high-spin states.

In this way, we are not able to reproduce the observed excitation energy, which shows the characteristic feature of the transverse wobbling decreasing as a function of spin. We have only tried the multiranked configuration mixing with respect to the cranking about the  $x$  axis. However, there is the possibility to mix configurations with cranking about all three axes, although the problem of the density-dependent term seems to appear for the Gogny (or Skyrme) interaction. Such a possibility is

interesting to be explored with different effective interactions, although it requires much heavier numerical efforts.

#### IV. SUMMARY

In the present work, we have investigated the nuclear rotational motion in triaxially deformed nuclei by employing the fully microscopic framework of angular-momentum projection from the mean-field wave function. As the first part of investigation, we have concentrated on the nuclear wobbling motion, which is quantized rotational motion of the rigid rotor. By employing the triaxially deformed mean-field wave function, we have confirmed that the characteristic energy spectrum of the multiple-band structure naturally emerges in the nucleus  $^{163}\text{Lu}$  by our projection calculation. Using the deformation parameters consistent with the Nilsson-Strutinsky calculation [43], a reasonable excitation energy is obtained for the one-phonon wobbling band but the excitation energy of two-phonon band is too large. Note that the excitation energies decrease as functions of spin, i.e., the transverse wobbling behavior [20] comes out, though the spin dependence is slightly too strong compared with the experimental data. However, the obtained moments of inertia for the TSD bands in  $^{163}\text{Lu}$  are generally too small for the employed Hamiltonian of the Woods-Saxon potential and the schematic interaction. To improve the moments of inertia, we have performed infinitesimal cranking [14] to include the time-odd components into the mean fields. The moments of inertia increase but not enough and the excitation energy of the one-phonon band is too small compared with the experimental data. Therefore, we do not aim to fit the experimental data but rather perform explorational calculations to understand the general property of the nuclear wobbling motion from the microscopic view point.

By making use of the freedom to crank the mean field around all three intrinsic axes, we have investigated how the transverse wobbling picture appears and what are its implications. We have found that the dynamics of the angular-momentum vector in the intrinsic coordinate frame of the mean field are reflected by the excitation energies of the wobbling phonon band. Namely, the transverse-wobbling behavior, i.e., the decrease of the wobbling excitation energy as a function of spin, emerges when the nucleus starts to rotate around the alignment axis of

the odd particle, which is the axis with the intermediate moment of inertia. Increasing the spin, the rotational axis changes to the axis with the largest moment of inertia. The critical spin value for vanishing excitation energy of the one-phonon wobbling band corresponds to the transition point of changing the direction of the angular-momentum vector from the axis with the intermediate moment of inertia to the axis with the largest moment of inertia. Although the moments of inertia are not explicitly introduced in our microscopic framework, the calculated cranking inertias (Fig. 1) have the order  $\mathcal{J}_y > \mathcal{J}_x > \mathcal{J}_z$  for the medium, short, and long axes, respectively, which is needed for transverse wobbling. Note that the rotation around the axis with the intermediate inertia is known to be unstable for rotation of the rigid body without the alignment. The unusual decreasing behavior of excitation energy is most probably related to this fact.

As for the transition probabilities, the main conclusion is the same as in previous work [25,34,36]. With fixed triaxial deformation, the in-band  $B(E2)$  values are almost constant and the out-of-band  $B(E2)$  values decrease as a function of spin. The comparison of these calculated  $B(E2)$  values with the experimental data suggests that the triaxial deformation of the charge density predicted by the Nilsson-Strutinsky calculation [43],  $\gamma(\text{den}) \approx 11\text{--}12^\circ$  in Eq. (15), is too small. The decrease of the in-band  $B(E2)$  and possible increase of the ratio  $B(E2)_{\text{out}}/B(E2)_{\text{in}}$  observed in the experimental data may suggest that the triaxiality increases at higher spins [25]. The problem of the too large out-of-band  $B(M1)$  values compared with the experimental data remains also in the present angular-momentum-projection calculation.

For the wobbling motion in the  $^{163}\text{Lu}$  nucleus, the angular-momentum-projection calculations from the fully self-consistent HFB mean field have been also performed by employing the Gogny-D1S interaction. We have found deformed HFB states whose triaxiality is consistent with the one determined by the Nilsson-Strutinsky calculation, i.e.,  $\gamma(\text{den}) \approx 11\text{--}12^\circ$ . The resultant spectrum of the angular-momentum projection is very similar to the one obtained by the Woods-Saxon potential and the simple schematic interaction. This strongly suggests that the collective wobbling does not depend on the details of the effective interaction. It should, however, be stressed that the more elaborate multicranked configuration-mixing calculation around the short axis can reproduce the moments of inertia of the TSD bands in a good approximation. On the other hand, the wobbling-phonon excitation energies are not reproduced in this configuration-mixing calculation. In the present work, only the possibility of the one-dimensional cranking is explored because of the problem of the density-dependent term in the Gogny interaction. The possibilities of cranking around all three axes should be explored in future studies with different effective interactions.

It should be emphasized that the wobbling motion was predicted based on the macroscopic rotor model, and the predicted properties are nicely confirmed by our microscopic calculation. Thus, the present study suggests that the macroscopic rotor model picture is realized in a good approximation for triaxially deformed atomic nuclei. It is, however, noted that a quantitative description of the wobbling motion is not obtained in the present work, and further investigations are necessary to achieve its fully microscopic understanding.

- 
- [1] A. Bohr and B. R. Mottelson, *Nuclear Structure*, Vol. II (Benjamin, New York, 1975).
- [2] P. Möller, R. Bengtsson, B. G. Carlsson, P. Olivius, and T. Ichikawa, *Phys. Rev. Lett.* **97**, 162502 (2006).
- [3] M. J. A. de Voigt, J. Dudek, and Z. Szymanski, *Rev. Mod. Phys.* **55**, 949 (1983).
- [4] S. Frauendorf, *Rev. Mod. Phys.* **73**, 463 (2001).
- [5] S. C. Panchoi, *Exotic Nuclear Excitations*, Springer Tracts in Modern Physics Vol. 242 (Springer, Berlin, 2011).
- [6] S. W. Ødegård, G. B. Hagemann, D. R. Jensen, M. Bergstrom, B. Herskind, G. Sletten, S. Tormanen, J. N. Wilson, P. O. Tjøm, I. Hamamoto *et al.*, *Phys. Rev. Lett.* **86**, 5866 (2001).
- [7] T. Nakatsukasa, K. Matsuyanagi, M. Matsuzaki, and Y. R. Shimizu, *Phys. Scr.* **91**, 073008 (2016).
- [8] S. Frauendorf, *Phys. Scr.* (to be published).
- [9] S. Frauendorf and J. Meng, *Nucl. Phys. A* **617**, 131 (1997).
- [10] P. Ring and P. Schuck, *The Nuclear Many-Body Problem* (Springer, Berlin, 1980).
- [11] S. Tagami and Y. R. Shimizu, *Prog. Theor. Phys.* **127**, 79 (2012).
- [12] S. Tagami, Y. R. Shimizu, and J. Dudek, *Phys. Rev. C* **87**, 054306 (2013).
- [13] S. Tagami, Y. R. Shimizu, and J. Dudek, *J. Phys. G* **42**, 015106 (2015).
- [14] S. Tagami and Y. R. Shimizu, *Phys. Rev. C* **93**, 024323 (2016).
- [15] M. Shimada, S. Tagami, and Y. R. Shimizu, *Prog. Theor. Exp. Phys.* **2015**, 063D02 (2015).
- [16] M. Shimada, S. Tagami, and Y. R. Shimizu, *Phys. Rev. C* **93**, 044317 (2016).
- [17] K. Hara and Y. Sun, *Int. J. Mod. Phys. E* **4**, 637 (1995).
- [18] Y. Sun, *Phys. Scr.* **91**, 043005 (2016).
- [19] J. A. Sheikh, G. H. Bhat, W. A. Dar, S. Jehangir, and P. A. Ganai, *Phys. Scr.* **91**, 063015 (2016).
- [20] S. Frauendorf and F. Döna, *Phys. Rev. C* **89**, 014322 (2014).
- [21] S. Tagami, M. Shimada, Y. Fujioka, Y. R. Shimizu, and J. Dudek, *Phys. Scr.* **89**, 054013 (2014).
- [22] T. Bengtsson and I. Ragnarsson, *Nucl. Phys. A* **436**, 14 (1985).
- [23] S. Frauendorf, *Nucl. Phys.* **557**, 259c (1993).
- [24] R. Wyss (private communication).
- [25] T. Shoji and Y. R. Shimizu, *Prog. Theor. Phys.* **121**, 319 (2009).
- [26] E. R. Marshalek, *Nucl. Phys. A* **331**, 429 (1979).
- [27] N. Tajima, Y. R. Shimizu, and S. Takahara, *Phys. Rev. C* **82**, 034316 (2010).
- [28] J. F. Berger, M. Girod, and D. Gogny, *Comput. Phys. Commun.* **63**, 365 (1991).
- [29] A. Kerman and N. Onishi, *Nucl. Phys. A* **361**, 179 (1981).
- [30] R. E. Peierls and D. J. Thouless, *Nucl. Phys.* **38**, 154 (1962).
- [31] S. Åberg, *Nucl. Phys. A* **520**, 35c (1990).
- [32] H. Schnack-Petersen, R. Bengtsson, R. A. Bark, P. Bosettic, A. Brockstedt, H. Carlsson, L. P. Ekström, G. B. Hagemann, B. Herskind, F. Ingelbretsen *et al.*, *Nucl. Phys. A* **594**, 175 (1995).
- [33] G. B. Hagemann, *Eur. Phys. J. A* **20**, 183 (2004).
- [34] Y. R. Shimizu, T. Shoji, and M. Matsuzaki, *Phys. Rev. C* **77**, 024319 (2008).

- [35] M. Shimada, Ph.D. thesis, Department of Physics, Kyushu University, Fukuoka, Japan, 2016.
- [36] S. Frauendorf and F. Dönau, *Phys. Rev. C* **92**, 064306 (2015).
- [37] D. R. Jensen, G. B. Hagemann, I. Hamamoto, S. W. Odegard, B. Herskind, G. Sletten, J. N. Wilson, K. Spohr, H. Hubel, P. Bringel *et al.*, *Phys. Rev. Lett.* **89**, 142503 (2002).
- [38] A. Görge, R. M. Clark, M. Cromaz, P. Fallon, G. B. Hagemann, H. Hubel, I. Y. Lee, A. O. Macchiavelli, G. Sletten, D. Ward, and R. Bengtsson, *Phys. Rev. C* **69**, 031301 (2004).
- [39] Y. R. Shimizu, M. Matsuzaki, and K. Matsuyanagi, in *Proceedings of the Fifth Japan-China Joint Nuclear Physics Symposium* (Fukuoka, Japan, 2004), pp. 317–326.
- [40] M. Matsuzaki and S.-I. Ohtsubo, *Phys. Rev. C* **69**, 064317 (2004).
- [41] I. N. Mikhailov and D. Janssen, *Phys. Lett. B* **72**, 303 (1978).
- [42] I. Hamamoto, S. W. Ødegård, G. B. Hagemann, D. R. Jensen, M. Bergström, B. Herskind, G. Sletten, S. Törmänen, J. N. Wilson, P. O. Tjøm *et al.*, *Acta Phys. Pol. B* **32**, 2545 (2001).
- [43] R. Bengtsson and H. Ryde, *Eur. Phys. J. A* **22**, 355 (2004).
- [44] Y. R. Shimizu and M. Matsuzaki, *Nucl. Phys. A* **588**, 559 (1995).
- [45] J. Dobaczewski, M. V. Stoitsov, W. Nazarewicz, and P.-G. Reinhard, *Phys. Rev. C* **76**, 054315 (2007).
- [46] L. M. Robledo, *J. Phys. G* **37**, 064020 (2010).